

JGR Atmospheres

RESEARCH ARTICLE

10.1029/2023JD040679

Key Points:

- Space-time covariance can summarize the space-time structure of time-varying spatial fields of surface fluxes and states
- The observed space-time covariance of land surface temperature (LST) reveals variability in its characteristic length and time scales over the United States
- Clustering of the fitted LST space-time covariance parameters reveals the role of environmental characteristics in the observed patterns

Correspondence to:

L. Torres-Rojas,
laura.torres@duke.edu

Citation:

Torres-Rojas, L., Waterman, T., Cai, J., Zorzetto, E., Wainwright, H. M., & Chaney, N. W. (2024). A geostatistics-based tool to characterize spatio-temporal patterns of remotely sensed land surface temperature fields over the Contiguous United States. *Journal of Geophysical Research: Atmospheres*, 129, e2023JD040679. <https://doi.org/10.1029/2023JD040679>

Received 23 JAN 2024

Accepted 30 AUG 2024

Author Contributions:

Conceptualization: L. Torres-Rojas, N. W. Chaney

Data curation: L. Torres-Rojas, J. Cai

Formal analysis: L. Torres-Rojas, T. Waterman, J. Cai, E. Zorzetto, H. M. Wainwright, N. W. Chaney

Funding acquisition: N. W. Chaney

Investigation: L. Torres-Rojas

Methodology: L. Torres-Rojas, N. W. Chaney

Project administration: N. W. Chaney

Resources: H. M. Wainwright, N. W. Chaney

Software: L. Torres-Rojas, J. Cai, N. W. Chaney

Supervision: H. M. Wainwright, N. W. Chaney

Validation: L. Torres-Rojas, N. W. Chaney

Visualization: L. Torres-Rojas

Writing – original draft: L. Torres-Rojas

Writing – review & editing: L. Torres-Rojas, T. Waterman, J. Cai, E. Zorzetto, H. M. Wainwright, N. W. Chaney

© 2024. American Geophysical Union. All Rights Reserved.

A Geostatistics-Based Tool to Characterize Spatio-Temporal Patterns of Remotely Sensed Land Surface Temperature Fields Over the Contiguous United States

L. Torres-Rojas¹ , T. Waterman¹ , J. Cai¹, E. Zorzetto², H. M. Wainwright^{3,4}, and N. W. Chaney¹ 

¹Department of Civil and Environmental Engineering, Duke University, Durham, NC, USA, ²Program in Atmospheric and Oceanic Sciences, Princeton University, Princeton, NJ, USA, ³Lawrence Berkeley National Laboratory, Earth and Environmental Sciences Area, Berkeley, CA, USA, ⁴Massachusetts Institute of Technology, Cambridge, MA, USA

Abstract Surface fluxes and states can recur and remain consistent across various spatial and temporal scales, forming space-time patterns. Quantifying and understanding the observed patterns is desirable, as they provide information about the dynamics of the processes involved. This study introduces the empirical spatio-temporal covariance function and a corresponding parametric covariance function as tools to identify and characterize spatio-temporal patterns in remotely sensed fields. The method is demonstrated using 2 km hourly GOES-16/17 land surface temperature (LST) data over the Contiguous United States by splitting the area into $1.0^\circ \times 1.0^\circ$ domains. The summer day-time LST ESTCFs for 2018 to 2022 are derived for each domain, and a parametric covariance model is fitted. Clustering analysis is applied to detect areas with similar spatio-temporal LST patterns. Six main zones within CONUS are identified and characterized based on their variance and temporal and spatial characteristic length scales (i.e., scales for which the temperature variations are temporally and spatially related), respectively: (a) Eastern plains with $3 K^2$, ~ 6 hr, and 0.15° , (b) Gulf of California with $60 K^2$, ~ 8 hr, and 0.34° , (c) mountains and coasts transition 1 with $16 K^2$, ~ 11 hr, and 0.25° , (d) central US, Midwest, and South cities with $5.5 K^2$, ~ 8 hr, and $\sim 0.2^\circ$, (e) mountains and coasts transition 2 with $\sim 10 K^2$, ~ 8 hr, and 0.2° , and (f) largest mountains and coastlines with $\sim 19 K^2$, ~ 13 hr, and 0.3° . The tools introduced provide a pathway to formally identify and summarize the spatio-temporal patterns observed in remotely sensed fields and relate those to more complex processes within the Soil-Vegetation-Atmosphere System.

Plain Language Summary Specific processes on Earth's surface, like heat and water fluxes and air movement, often exhibit coherent patterns across space and time. Figuring out where these patterns occur can be helpful as they can aid to explain how the underlying physical processes work. This research introduces a new tool to find and describe these patterns and applies it to temperature data derived from satellites. The United States is divided into smaller areas, and the developed tool is used to analyze the land temperature data within those areas; then, regions with similar temperature patterns are identified. These results help to determine that certain landscape features, like coastlines, mountains, and cities, influence how temperature patterns behave in space, time and both. These tools help us to recognize and describe the patterns we see in satellite observations and ultimately, connect them to more complicated processes happening in the Soil-Vegetation-Atmosphere System.

1. Introduction

For climate, environmental, and hydrological applications, the simultaneous identification of spatially coherent persistent structures (i.e., spatio-temporal patterns) of surface states and fluxes is desirable, as they provide information about the dynamics of the processes affecting them. Generally, the spatio-temporal nature of these patterns is non-separable, as their spatial and temporal dimensions are highly intertwined (Faghmous & Kumar, 2014). For instance, let us consider the distribution of inundation in a flood-prone area. Multiple processes determine the inundation dynamics within a watershed, including the spatio-temporal distribution of precipitation, watershed-distributed physical characteristics (i.e., soil properties, antecedent soil moisture content (SMC)), and human modifications. The spatio-temporal evolution of the flooding as it moves downstream due to re-infiltration, evaporation, preferential flow, and other processes would be missed by looking only at the spatial or temporal dimensions independently (Cressie & Wikle, 2015). Another case where the simultaneous space-time evolution of variables is pivotal for process understanding is the initiation of heterogeneity-driven atmospheric

circulations at multiple scales. Under favorable atmospheric boundary layer (ABL) and synoptic background conditions, larger spatial scales of surface heterogeneity can generate temporally persistent structures of surface heating and moisture, initiating circulations that, for large enough scales, can increase the likelihood of shallow or even deep convection (F. Chen & Avissar, 1994; Cheng & Cotton, 2004; Courault et al., 2007; Gentile et al., 2019; Pielke, 2001; Taylor et al., 2007; Weaver, 2004; C. Wu et al., 2015). The two previous examples highlight the need for approaches that succinctly and effectively identify and summarize the spatio-temporal patterns observed in climatic, environmental, and hydrological data sets.

Several statistical approaches have been developed to identify, summarize, and extract relevant patterns from spatio-temporal geophysical data sets. The reader is referred to (Cressie & Wikle, 2015; Vereecken et al., 2016) for a detailed exploration of some of these approaches, their advantages, and their information content. Most approaches are based on decomposing the spatial and temporal signals according to their statistics or scales. Examples of decomposition approaches include the Empirical Orthogonal Function (EOF) method, also known as Principal Component Analysis (PCA) by statisticians, unsupervised classification (i.e., clustering), Orthogonal Probability Density Function Decomposition (OPDFD), Wavelet Transform (WT), Empirical Mode Decomposition (EMD), and Ensemble Empirical Mode Decomposition (EEMD). These approaches can be applied in space and/or time and have proved to be helpful in the simplification of complex data sets, the decomposition and identification of relevant spatial and temporal signals, and the determination of critical scales of processes within the Soil-Vegetation-Atmosphere System (SVAS) (Biswas, 2014; Z. Fang et al., 2015; Graf et al., 2012; Katul & Parlange, 1995; Katul et al., 2001; Kim & Barros, 2002; Koch et al., 2015; Korres et al., 2010; Rudi et al., 2010; Stoy et al., 2005; Vargas et al., 2010; D. Wagner et al., 1990). However, some of these approaches are only meant to analyze time or space dimensions independently (i.e., EOF and EMD), assume spatial and temporal dimensions as separable (i.e., EEMD and clustering) (Z. Wu et al., 2016), and often encounter challenges providing a physical meaning for their results (i.e., clustering, PCA, OPDFD, EEMD) (Dommegent & Latif, 2002; Hannachi et al., 2007; Monahan et al., 2009). Finally, all approaches display challenges in representing non-stationary processes and computational issues affecting the analysis of almost all large-scale environmental data sets (Kuusela & Stein, 2018).

Geostatistical theory, developed to model the variability of geophysical and environmental regionalized variables, stands as a straightforward alternative to relatively complex decomposition approaches. In geostatistics, it is assumed that expected values of the variables are spatio-temporally dependent, meaning that data points close to each other are more similar than data points at larger spatio-temporal distances (Tobler, 1970; van der Meer, 2012; Vereecken et al., 2016). Observations are considered realizations of a random process where the variable has a spatial and temporal dependence structure that can be modeled. The modeled dependence structure has found extensive applications in prediction in space (i.e., smoothing or interpolation), prediction in time (i.e., forecasting), downscaling, mapping, and designing sampling of in situ data. For specific examples of these applications, the reader is referred to van der Meer (2012), Wikle (2015), and Zakeri & Mariethoz (2021). Even though geostatistical theory can make significant assumptions about the characteristics of the spatio-temporal fields and associated patterns (i.e., stationarity, spatio-temporal dependence, isotropy, and homoscedasticity, among others), it is still widely used as a compact and straightforward evaluation method of the structure of the observation fields. Moving window sampling (MWS) techniques have been implemented to deal with the stationarity assumption: while environmental phenomena exhibit heterogeneity in both their mean and covariance structure, it is often possible to regard the process as approximately homogeneous within subregions (Guttorp & Sampson, 1994; Haas, 1990a, 1990b; Kuusela & Stein, 2018; Risser & Turek, 2020). Moving window sampling (MWS) results in spatially variable assessments of the spatio-temporal dependence structure based on data, providing results that reflect the non-stationarity of the underlying random fields. Additionally, MWS is computationally efficient, as it processes only a subset of the complete data set at any given time and allows for full parallelization of the computation windows (Kuusela & Stein, 2018). Finally, MWS is highly flexible and has the advantage of providing with localized assessments of the spatio-temporal structure of fields without being limited by the domain shape or size, except for sampling purposes.

A straightforward approach that comes from classical geostatistics in space and time is the covariance function. It provides measures of the strength and structure of dependence between values at different locations and time points as a function of the spatio-temporal separation. It can be derived either from a fitted stochastic model or inferred from the empirical covariance of the data (i.e., empirical spatio-temporal covariance function (ESTCF)). Under the assumptions of second-order stationarity in space and time (i.e., the covariance between two points is

the same for a given distance and direction, regardless of which two points are chosen) and isotropy in space, the ESTCF can be estimated directly from the observed data (W. Chen et al., 2021; Cressie & Huang, 1999; Faghmous & Kumar, 2014; Gneiting, 2002; Stein, 2005). The ESTCF is also able to capture various forms of dependence, such as spatial correlation, temporal correlation, and spatio-temporal interactions (Cressie & Huang, 1999; Gneiting, 2002; Guttorp & Sampson, 1994; Ma, 2003; Stein, 2005). Finally, the ESTCF can handle irregularly sampled data or missing values more effectively than other statistical approaches (e.g., spectral analysis), making it more suitable for real-world applications where data may be sparse or irregularly collected (Demel & Du, 2015; Montero et al., 2015; Stein, 1999). When a closed form of a stochastic model is unavailable, or observations are too sparse to compute the ESTCF, a common practical approach is to choose a covariance function from a parametric family with members known to be positive-definite functions (W. Chen et al., 2021; Gneiting, 2002; Ma, 2005). Ideally, the selected covariance function structure should respond to what is quantitatively known about the system physical dynamics. However, in reality, the knowledge of the system might be limited, and the structure of the function and parameter values must be tailored to reflect the dependence structure of the observed underlying physical field (Kuusela & Stein, 2018). The reader is referred to (Cressie & Huang, 1999; Cressie & Wikle, 2015; Montero et al., 2015; Stein, 2005) for a comprehensive review of some of the available parametric model structures.

A comprehensive geostatistical exploration of the space-time dependence structure for any variable requires high-resolution data in both space and time (Stein, 2020). Although this analysis is possible with contemporary spatially distributed hydrologic and land surface models (e.g., Chaney et al., 2016), it remains a challenge using in-situ data due to the lack of widespread, long-term, high-resolution, spatially distributed in-situ observations of surface fluxes and states (Stisen et al., 2011, 2021; Vereecken et al., 2008; Zink et al., 2018). Hence, satellite remote sensing remains the only direct source of long-term, spatially distributed Earth surface observations. Although the quantitative precision of this data is still hard to determine, its main asset is its spatial and temporal information content over extensive domains (Crow et al., 2009; H. T. Li et al., 2009; Stisen et al., 2011). Currently, sensors onboard satellites provide spatially distributed estimates of several surface states, including land surface temperature (LST) (L. Fang et al., 2014; Shi & Bates, 2011; Wan, 2014; Wan & Dozier, 1996; Yu et al., 2012), SMC (Chan et al., 2018; Entekhabi et al., 2010; Kerr et al., 2012; Parinussa et al., 2015; W. Wagner et al., 2013), evapotranspiration (Boschetti et al., 2019; J. B. Fisher et al., 2020; Martens et al., 2017; Running et al., 2019; Su, 2002), snow cover fraction (Painter et al., 2009; Tsai et al., 2019), and changes in water storage (Tapley et al., 2004). This availability of observations reduces the need for data prediction/interpolation, permitting to focus on inferring spatio-temporal properties of the available variables. For instance, Kuusela and Stein (2018) proved how local estimation of covariance function parameters for sea temperature along latitudes and longitudes agree with known features of processes. Therefore, the joint use of the ever-growing available remote sensing spatio-temporal data and geostatistics provides a promising path forward in the multi-scale characterization of the heterogeneity of processes and dynamics in multiple compartments of the SVAS.

One especially promising variable for studying land surface processes is LST (Duffy et al., 2022; Koch et al., 2016; Zink et al., 2018). As a critical state variable of the land surface, LST encodes information on local energy and water fluxes, including energy partitioning into sensible and latent heat fluxes (Duffy et al., 2022; Holzman et al., 2014; K. Li et al., 2021; Sims et al., 2008; K. Wang & Dickinson, 2012). This information is vital as energy partitioning can affect the state of the atmosphere by supplying water vapor, inducing convection and lateral convergence, and growing the planetary boundary layer (Levine et al., 2016; Pielke, 2001; Tuttle & Salvucci, 2016). Additionally, Simon et al. (2021) showed that accounting for the spatial patterns of sensible heat flux, a surface flux tightly coupled to LST, plays a crucial role in driving the atmospheric response to land surface heterogeneity. Recently, enhanced spatio-temporal resolution global LST products have been released, including the ECOSystem Spaceborne Thermal Radiometer on the International Space Station (ECOSTRESS) (Hook & Hulley, 2019), Landsat Provisional (Anderson et al., 2012), the National Oceanic and Atmospheric Administration (NOAA) Geostationary Operational Environmental Satellites (GOES) (L. Fang et al., 2014; Yu et al., 2012), and Sentinel-3 (Polehampton et al., 2022). However, increased spatial resolutions are often not accompanied by enhanced temporal resolutions. Products derived from sensors onboard satellites with polar orbits, such as NASA's Moderate Resolution Imaging Spectroradiometer (MODIS), are accurate and extensively validated. However, due to the nature of the satellite orbit and the intermittency of the revisit times, the temporal resolution of the resulting products is limited, and diurnal and sub-diurnal variations cannot be captured. On the other hand, sensors onboard geostationary satellites (e.g., GOES) remain in fixed positions overlooking the Earth,

providing full disk observations every 10 min. Geostationary satellites also provide increased robustness to cloud coverage (Duffy et al., 2022; Hashimoto et al., 2021), a desirable feature for the study of atmospheric motions generated by landscape discontinuities (F. Chen & Avissar, 1994). The possibility to explore the dynamics in space and time (i.e., movies) of LST at the diurnal cycle using succinct summaries like the space-time covariance function is a unique opportunity, particularly in the study of land-atmosphere interactions (Dickinson, 1995; Entekhabi, 1995; Gentile et al., 2019; Nicholson, 1988; Santanello et al., 2018).

This study introduces the ESTCF as a tool to assess the spatial coherence (i.e., spatial characteristic length scale) and memory (i.e., temporal characteristic length scale) of remotely sensed spatio-temporal fields and identify patterns that might be relevant in the dynamics of processes within the SVAS. Additionally, the study presents a new 4-parameter covariance function model to summarize the spatio-temporal structure displayed by the ESTCF and provides physical interpretations for its parameters. These tools are applied to remotely sensed fields of sub-diurnal LST to evaluate whether they can identify areas where landscape features (e.g., coastlines, topographic gradients, and urban areas, among others) might be responsible for triggering surface heterogeneity-driven atmospheric circulations. These developments are implemented and tested over CONUS by using a computationally efficient MWS approach, splitting the entire country into a mosaic of $1.0^\circ \times 1.0^\circ$ domains, deriving the summer day-time surface temperature ESTCF for each domain independently, and fitting the parametric covariance function model to each specific domain. Once the parametric covariance functions for all domains are known, clustering analysis is applied to the obtained parameter maps in order to detect areas with similar spatio-temporal surface temperature dynamics. The key developments in this study include (a) a flexible and comprehensive tool to characterize and represent the spatio-temporal dependence structure of remotely sensed fields, (b) a parametric covariance function model to more concisely describe the spatio-temporal patterns captured with the ESTCF, (c) a multi-dimensional clustering approach to determine areas with similar spatio-temporal dependence structures, and (d) data-driven local estimates of the spatial, temporal and spatio-temporal dependence scales for LST over CONUS. The tools introduced here provide a pathway forward to formally identify and summarize the spatio-temporal patterns observed in remotely sensed fields and relate those to the footprint of more complex dynamic processes within the SVAS. The methods and results sections focus on computing the space-time covariance from the data and then analyzing them via spatial maps of parameters as well as clustering maps; the potential implications for land-atmosphere interactions are discussed in more detail in the discussion section.

2. Data and Methods

2.1. Data

2.1.1. GOES-16 LST and Sea Surface Temperature (SST)

The NOAA's GOES are the latest and main operational geostationary weather satellites in orbit over the Western hemisphere (Desai et al., 2021). Recently, the GOES-R Advanced Baseline Imagers (ABIs) on board the new generation GOES-16 and GOES-17 satellites have been generating an LST operational product based on scans at roughly 5 min with an approximate 2 km spatial granularity over the continental United States (CONUS). The GOES ABI LST estimates are produced using a thermal channel split-window retrieval based on the bands centered at 10.8 and 12.3 μm with high surface emission and low atmospheric absorption. Additionally, the algorithm uses a prescribed surface emissivity and an atmospheric radiative transfer model. For further details on the retrieval algorithm, the reader is referred to (Yu & Yu, 2020). The final operational product has been generated at an hourly time scale from May 2017 to the present. Evaluations have shown that the product is high quality, with validation studies indicating an approximate accuracy of 1.5 K (Chang et al., 2021; Desai et al., 2021; Yu et al., 2012). Given the characteristic spatial and temporal scales reported for mesoscale heterogeneity-driven circulations, it is expected that GOES-16 provides an observational source with both sufficiently high spatial resolution (i.e., ~ 2 km over CONUS) and high temporal resolution (i.e., 1 hr) to perform the subsequent analyses.

A SST product is also produced from the ABI retrievals on board the GOES satellites. The ABIs on board GOES-16 and 17 offer improved capabilities for SST retrievals, over its predecessors, including five narrow bands that can be used to estimate SST. Other advantages include accurate sensor calibration, image navigation and co-registration, spectral fidelity, and sophisticated preprocessing. Using this information, the Level 2 Pre-processed (L2P) SST product is derived at the native sensor resolution (2 km at nadir, degrading to 15 km at view zenith angle, 67°) using NOAA Advanced Clear-Sky Processor for Ocean (ACSPO) system (Ignatov et al., 2019).

SST is derived from the original 10-min full-disk brightness temperatures using the ACSPO clear-sky mask (Petrenko et al., 2010) and the Non-Linear SST algorithm (Petrenko et al., 2014). Four longwave bands centered at 8.4, 10.3, 11.2, and 12.3 μm are used. The regression is calibrated against quality-controlled in situ SST observations from drifting and tropical mooring buoys in the NOAA iQuam system (Xu & Ignatov, 2014). Finally, the 10-min full-disk data is unified in time to produce the 1-hr L2P product, with improved coverage and reduced cloud leakages and image noise, compared to each 10-min image.

Given the interest to explore the spatio-temporal patterns of remote sensing LST that can lead to the development of heterogeneity-driven atmospheric circulations, coastal regions are relevant (e.g., land-sea breezes are one of the most evident examples of an increased land-atmosphere coupling strength). In this sense, a LST product alone is insufficient to perform the analysis; an SST product must also be used. For this study, the hourly GOES-16 LST data over CONUS is superimposed on the hourly GOES-16 SST data over the Americas region from January 2018 to December 2022. The resulting 1-hr, 2-km, CONUS-wide surface temperature data set is then bounded to only consider pixels containing at least 30% of land in their area. This data set is then used to determine the spatio-temporal dependence structure of the LST fields in different domains. The obtained structures are expected to show consistent behaviors in places where landscape features can contribute to generating heterogeneity-driven circulations. We acknowledge that differences in the algorithms used to retrieve SST and LST might generate inconsistencies in the values between water and land in the consolidated LST data set. However, the main reason for merging the data is to analyze the contrasting temperatures in coastal patches that would be impossible to analyze using an LST product alone.

It is well established that atmospheric motions influenced by landscape discontinuities develop mainly during summer daytime hours and are optimum under clear sky conditions (F. Chen & Avissar, 1994). For this reason, analyses in this study use only warm months (i.e., June, July, August, and September), daytime hours, and clear-sky pixels of the LST data set. Daytime hours are determined locally for each individual domain over CONUS (see Section 2.2) as the period between 2 hr after sunrise and 2 hr before sunset. The raw GOES-LST and GOES-SST data sets are provided in the native ABI fixed grid coordinates; therefore, reprojection to the WGS84 projection (i.e., EPSG:4326) is implemented before further analyses.

2.1.2. Related Physical Covariates

An analysis of some landscape variability features of the analyzed domains is performed to determine some static physical and climatological characteristics that might relate to the LST spatio-temporal dynamics. For the analysis, a stack of high-resolution open-access environmental data sets for topography, land cover, and climatology are used to assess the spatial standard deviation of the properties inside $1^\circ \times 1^\circ$ domains (as shown in Figure 1). The selected data sets attempt to represent multiple sources of static physical heterogeneity known to affect the spatio-temporal dynamics of surface temperature through shading (e.g., elevation and tree cover fraction), albedo (e.g., land cover), and climatological variability (e.g., precipitation, incident radiation, and air temperature). This multivariate data set does not attempt to capture all possible physical sources of variability for surface temperature but provides a first-order assessment of the potential dominant features. The specifications of the data sets used in this study are presented in Table 1. The products include the one arcsec (~ 30 m) USGS National elevation data set (NED), the one arcsec (~ 30 m) National Land Cover Database (NLCD), the one arcsec (~ 30 m) 2015 Global Forest Cover Change (GFCC) Tree Cover Multi-Year Global data set and the 30 arcsec (~ 800 m) Parameter-elevation Regressions on Independent Slopes Model (PRISM) data set, that provides 30-year climatologies of relevant variables (Daly et al., 1997; Gesch et al., 2010; Homer et al., 2015; Rupp et al., 2022; Townshend, 2016).

The maps presented in Figure 1 are directly obtained from computing the standard deviation of selected physical characteristics on $1^\circ \times 1^\circ$ subdomains (as described in Section 2.2.2): Figure 1a presents elevation from NED, Figures 1b–1d PRISM precipitation climatology, PRISM air temperature climatology, and PRISM shortwave downward sloped solar radiation climatology, respectively, and Figure 1e tree cover fraction from GFCC. Figures 1f–1i are all derived from NLCD by assigning a value of 1 to pixels containing a certain land cover type (i.e., water, urban, forest, and bare soil) and 0 to all pixels not containing those values; then, the standard deviation inside each domain is computed over the obtained classes maps. Since the spatial extent of all the data sets is not the same (i.e., some are meant to analyze only US territories while others are global), only subdomains containing information of all the data sets are considered in the analysis.

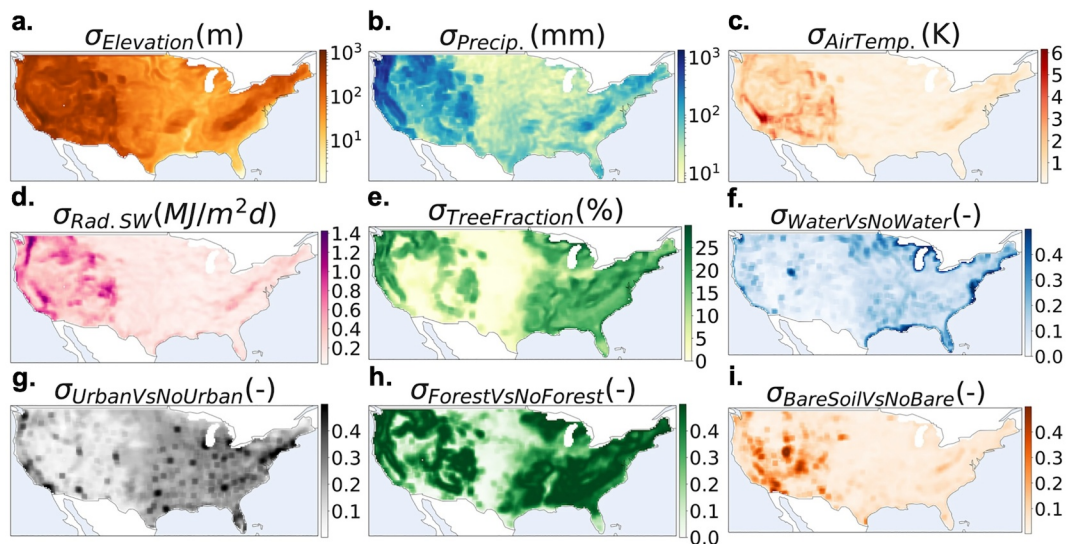


Figure 1. Maps of standard deviation of physical features for land-containing domains. Each pixel represents the central $0.25^\circ \times 0.25^\circ$ for each $1.0^\circ \times 1.0^\circ$ analyzed domain. (a) Elevation standard deviation, (b) precipitation climatology, (c) air temperature climatology, (d) shortwave downward solar radiation, (e) tree cover fraction, (f) water versus no water, (g) urban versus no urban, (h) forest versus no forest, and (i) bare soil versus no bare soil.

2.2. Methods

2.2.1. ESTCF

The summer, daytime ESTCF of LST between 2018 and 2022 is computed for all the $1.0^\circ \times 1.0^\circ$ subdomains across the country (see Section 2.2.2 for details on the subdomain definition). The objective is to summarize and characterize the long-term spatio-temporal dynamics of the LST fields in subdomains across CONUS.

The ESTCF expresses how the linear statistical dependence of two measurements in a spatio-temporal random field reduces as the distances (in space and time) between them increase, up to the lengths of statistical independence where a relation no longer exists and the covariance tends to zero (Cressie & Wikle, 2015; Mälicke et al., 2020). The spatio-temporal dependence structure displayed by the observed realizations is summarized using the ESTCF. The mathematical procedure used to compute the ESTCF for a random field is presented next and explained based on (Montero et al., 2015).

Let $Z(\cdot, \cdot)$ be an intrinsically stationary process observed on a set of n spatio-temporal locations $\{(s_1, t_1), \dots, (s_n, t_n)\}$ where s_i is the spatial location and t_j the observation time. The classical alternative to estimate the empirical covariance function using the observed values if the process is second-order stationary is proposed by Mathérón (1989). This classical estimation is obtained by implementing the Method-of-Moments estimator (MoM), which for the covariance function takes the form:

Table 1
Specifications of Environmental Data Sets Used in the Study

Group	Parameter	Data source	Period	Spatial resolution (m)	References ^a
Thirty-year climatology	Precipitation	PRISM	1991–2020	~800	Daly et al. (1997) and Rupp et al. (2022)
	Short wave radiation				
	2 m air temperature				
Land cover	Land cover classification	NLCD	2016	30	Homer et al. (2015)
Topography	Elevation	NED	–	30	Gesch et al. (2010)
Tree cover	Tree cover fraction	GFCC	2015	30	Townshend (2016)

^aAll the data sets are open access and available at the provided references.

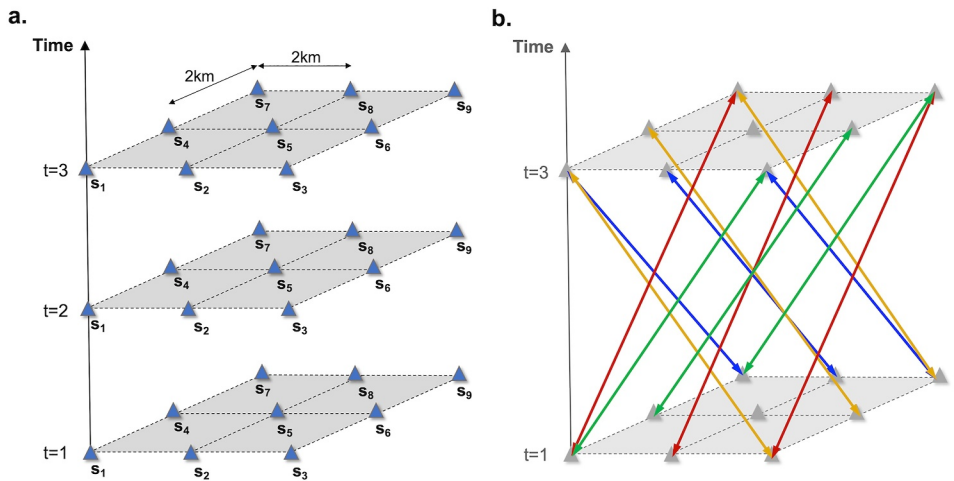


Figure 2. (a) Schematic view of a regularly-spaced 2-km grid over a time axis with 3 compartments; (b) 12 pairs of points separated by a spatial distance of 4 km and a temporal lag of 2 ($(h, u) = (4 \text{ km}, 2)$), colors represent sides of the spatial grid where the origin point is located: yellow for left, red for back, green for right, and blue for front.

$$C(h(l), \tau(k)) = \frac{1}{\#N(h(l), \tau(k))} \sum_{\substack{(s_i, t_i), (s_j, t_j) \\ \in N(h(l), \tau(k))}} (Z(s_i, t_i) - \bar{Z}_{t_i})(Z(s_j, t_j) - \bar{Z}_{t_j}) \quad (1)$$

Where $\bar{Z}_i = \frac{1}{n} \sum_m Z(s_m, t_i)$ is an estimator of the mean μ_i of the random field for the time t_i and $N(h(l), \tau(k)) = \{(s_i, t_i) : s_i - s_j \in T(h(l)), t_i - t_j \in T(\tau(k))\}$, where $T(h(l))$ is the tolerance region on \mathbb{R}^d around $h(l)$, $T(\tau(k))$ is the tolerance region on \mathbb{R} around $\tau(k)$, and $\#N(h(l), \tau(k))$ is the number of different elements in $N(h(l), \tau(k))$, with $l = 1, \dots, L$ and with $k = 1, \dots, K$.

In general, the areas $T(h(l))$ and $T(\tau(k))$ are chosen to yield disjoint sets with enough elements to generate stable estimates. Suppose the hypothesis of isotropy is reasonable for the spatial process under analysis. In that case, the area of spatial tolerance around each of the values $h(l)$ can be defined as $[h(l) - d_l/2, h(l) + d_l/2]$, with d_l being the spatial tolerance to be used. Also common is to make the temporal component take values in \mathbb{Z} , in which case the empirical covariance function is computed for $\tau(k) = 0, 1, \dots$, obtained as the subsequent differences in time at which the process is observed. To better illustrate the described procedure, a simplified example is included next.

Let us suppose there is a set of spatio-temporal measurements taken at three points in time, t_1 , t_2 , and t_3 , on a regular grid of size 3×3 with a spacing of 2 km (Figure 2a). Assuming the resulting spatio-temporal random field is isotropic and stationary and that tolerance regions are not used, the classical ESTCF will be given by the simplified form of Equation 1:

$$C(h, \tau) = \frac{1}{\#N(h, \tau)} \sum_{N(h, \tau)} (Z(s_i, t_i) - \bar{Z}_{t_i})(Z(s_j, t_j) - \bar{Z}_{t_j}) \quad (2)$$

In this example, it is easy to show that there are $9 \times 3 = 27$ spatio-temporal points at a distance $(h, \tau) = (0 \text{ km}, 0)$. Therefore, for Equation 2, $\#N(h, \tau) = 27$. By definition, $C(0 \text{ km}, 0)$ is the spatio-temporal variance of the random field, σ^2 .

Suppose the distance is $(h, \tau) = (0 \text{ km}, 1)$, then $\#N(h, \tau) = 9 \times 2 = 18$. Finally, if the distance is $(h, \tau) = (0 \text{ km}, 2)$, $\#N(h, \tau) = 9 \times 1 = 9$. If the empirical covariance is computed for all the previously defined spatio-temporal distances, the purely temporal empirical covariance function is obtained (i.e., only time varies). It is also trivial to prove that: $\#N(2 \text{ km}, 0) = 12 \times 3 = 36$ and $\#N(4 \text{ km}, 0) = 6 \times 3 = 18$. If the empirical covariance is computed just for the distances $(h, 0)$, the purely spatial empirical covariance is obtained. Additionally, cases where both the spatial and temporal lags are different from zero, can also be considered, though the pairs of points must be determined carefully. For instance, Figure 2b shows the 12 pairs of points separated by a spatio-temporal distance

$(h, u) = (4 \text{ km}, 2)$. It is important to mention that this procedure does not consider diagonal spatial distances for simplicity.

Since the produced LST data set already uses a regular spatio-temporal grid, the procedure described for the example is directly applied. As mentioned before, only clear sky, summer daytime pixels are used for the analysis in this work. If one or both points contained in any pair used to compute the ESTCF contain a missing value, the pair is ignored from the summation in Equation 2, and $\#N$ is modified accordingly by subtracting one. Additionally, to determine the spatial separation between points, h , each pixel is assigned its central coordinates in degrees.

Two conditions are implemented regarding the spatial distribution and number of missing values of the LST data set within each subdomain for every time step (i.e., quality control): (a) the average latitude and longitude of the LST valid pixels within the subdomain has to be within a range of $\pm 0.15^\circ$ of the central latitude and longitude of box, as a guarantee of centrality in the observations within the subdomain; otherwise, the time step LST values for the subdomain are considered missing and; (b) the fraction of missing LST values within each subdomain per time step cannot be higher than 0.25, to ensure a large enough sample of observations; otherwise, the time step values are considered missing.

Figure 3 summarizes the process to obtain the ESTCFs for each $1^\circ \times 1^\circ$ subdomain over CONUS. The figure includes a graphic description of the original CONUS-wide LST data set described in Section 2.1.1, the MWS and extraction of summer, daytime LST values for each subdomain, described in Section 2.2.2, and the quality control and ESTCF computation described in this section (Section 2.2.1).

2.2.2. Study Domain and MWS

Figure 4a shows the study domain used over CONUS, considering only the $1.0^\circ \times 1.0^\circ$ subdomains containing at least 30% of land in their area. The central 0.25° of each $1.0^\circ \times 1.0^\circ$ squared box obtained from the sliding window approach (introduced below) is presented in green. Coordinates every 5° are also displayed to aid in georeferencing. The selected CONUS-wide study domain has boundaries in 124.99°W , 64.83°W , 23.88°N , 50.92°N .

A sliding window approach is applied to the constructed LST data set over CONUS to deal with the inherent limitations of the stationarity assumption of the selected geostatistics method. The approach works by first defining a subdomain of size $1.0^\circ \times 1.0^\circ$ and then moving it over the remotely sensed field by a distance of 0.25° in the zonal and meridional directions, as shown in Figure 4b. The $1.0^\circ \times 1.0^\circ$ box size is determined as a typical resolution used in ESMs and General Circulation Models. For each position of the box, the whole spatio-temporal field of observations over summer daytime is retrieved (as shown in Figure 3). By adopting this approach, a comprehensive analysis is performed as different combinations of landscape features are considered, and it can be assumed that the stationarity assumption holds if LST is characterized as approximately homogeneous within the subdomains. The overlap of the nearby subdomains results in smoothly varying local estimates of the later fitted covariance function model parameters.

2.2.3. Sensitivity of ESTCFs to Sampling

The obtained ESTCF for each subdomain is largely impacted by the chosen limits for quality control affecting the spatio-temporal sampling (i.e., centrality threshold and maximum missing value fraction per time step) as well as by the used time period, or temporal sampling. However, there is still limited knowledge on how changes in those will ultimately influence the resulting covariance structure. A sensitivity analysis is thus performed to understand the individual effect of the spatio-temporal sampling in the resulting ESTCF for seven subdomains. The effects are evaluated both visually and through two metrics computed with respect to the baseline ESTCF, obtained using the thresholds defined in Section 2.2.1 and the full record period, 2018–2022. The two selected metrics are (a) root mean square error (RMSE) and (b) mean bias (mBIAS). Five scenarios, including the baseline simulation, are evaluated as described in Table 2.

2.2.4. A Parametric Model for the Spatio-Temporal Covariance Function

Once the ESTCF is computed for every subdomain in CONUS, a parametric model is fitted to it to summarize the results even further. Additionally, the obtained parameters are used to determine the similarity in the spatio-

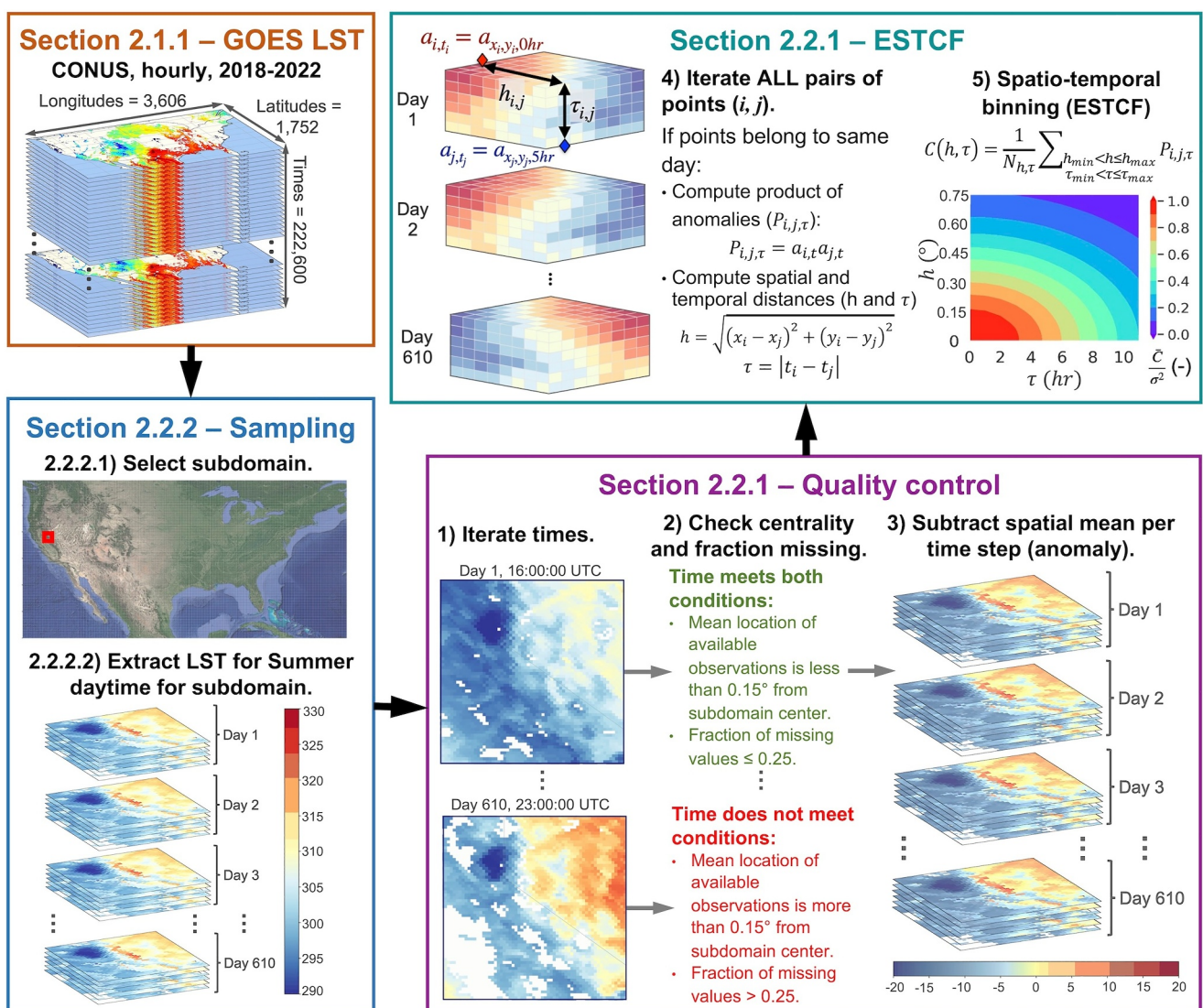


Figure 3. Flowchart summarizing the method for determining the land surface temperature empirical spatio-temporal covariance function for each $1^\circ \times 1^\circ$ sub-domain over CONUS. The approach relies on three interacting main stages as described in Sections 2.1.1 and 2.2.

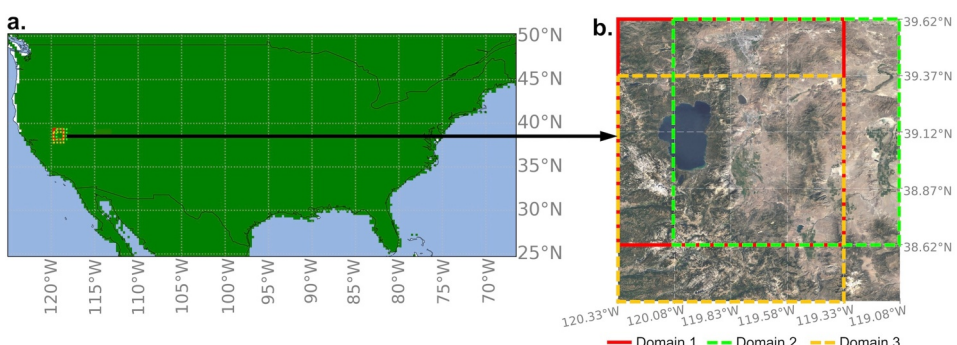


Figure 4. Study domain over CONUS and detail of the sliding window approach used. (a) Study domain over CONUS; the central 0.25° of each $1.0^\circ \times 1.0^\circ$ squared subdomain obtained from the sliding window approach is presented in green; coordinates every 5° are presented to aid in georeferencing. (b) Detail of the sliding window approach used for sampling over a subdomain in the California-Nevada border. Three $1.0^\circ \times 1.0^\circ$ subdomains separated by 0.25° from subdomain 1 in the horizontal (subdomain 2) and vertical (subdomain 3) directions are displayed.

Table 2

Sensitivity Analysis Scenarios Tested Including Spatial Centrality Threshold, Maximum Missing Fraction per Time Step and Time Period of Observations Used for Empirical Spatio-Temporal Covariance Function Computation

Scenario	Centrality threshold ($^{\circ}$)	Max. Missing fraction (-)	Time period
1	0.15 (baseline)	0.25 (baseline)	2018–2022 (baseline)
2	0.05	0.10	2018–2022
3	0.20	0.50	2018–2022
4	0.15	0.25	2018–2020
5	0.15	0.25	2018, 2020, 2022

temporal dependence structures between subdomains. This analysis is possible and informative only by summarizing the main features of the space-time covariance function in a limited number of parameters.

As mentioned in the Introduction section, the end goal of this study is not predicting LST but rather the characterization of the spatio-temporal dynamics of the LST fields within the subdomains. In this sense, the positive-definite nature of the selected parametric model is not a requirement since it is not used for Kriging. However, it is desirable that the chosen model uses a reduced number of parameters to facilitate optimization, minimize parameter equifinality (Beven, 2006), and enable physical interpretation of the parameters. For this reason, a modified form of the non-separable parametric model presented by Cressie and Huang (1999) is selected:

$$C(h, u) = \sigma^2 e^{-\left(\frac{u^a}{\gamma}\right) - \left(\frac{h^a}{\lambda}\right)} \quad (3)$$

where $C(h, u)$ is the parametric covariance at a spatio-temporal distance (h, u) ; σ^2 is the spatio-temporal variance of the random field, computed directly from the data; γ is the fitted temporal characteristic length-scale; λ is the fitted characteristic spatial length-scale; and a is the fitted spatio-temporal interaction exponent. Several other parametric models were tested on the available data, but the one selected showed improved performance with the lowest number of parameters.

2.2.5. Impact of the Parameters in the Spatio-Temporal Covariance Parametric Model

In the selected parametric covariance function model, the space-time interaction exponent (a) determines the shape of the space-time interaction, while the characteristic length scales (i.e., γ and λ) modify the magnitude of the spatial and temporal distances after they have been affected by the exponent (i.e., patches size and patches memory in time). Figure 5 displays the parametric spatio-temporal covariance functions obtained as the values of the parameters are successively modified. The figure allows us to see how:

- Larger values of the characteristic temporal length scale, γ , correspond to longer memory (see Figure 5c). In other words, for the produced parametric model, high covariance values are bound to persist longer in time as γ increases. When fitted to an observational data set, a high value of γ implies that the variable patterns (i.e., similar temperature patches) tend to remain for longer at the given location. The opposite behavior (i.e., shorter memory) can also be achieved by reducing γ , as observed in Figure 5a.
- Increased spatial memory of the modeled covariance function is achieved by raising the spatial length scale, λ (see Figure 5f). A fitted high λ suggests a large spatial coherence of the spatial patterns in the domain. In that case, the values of the observations for two points far from each other are highly correlated. The contrasting case (i.e., smaller spatial patches of similar temperature) can be modeled by decreasing λ , as presented in Figure 5d.
- Higher values of the space-time interaction exponent, a , lead to an increased interaction between space-time in the computed covariance function. The space-time interaction is directly related to the shape of the curves in the modeled covariance function. As a rises over one (see Figure 5i), the interaction between space and time becomes stronger, and the modeled transition between the pure-spatial and pure-temporal covariance occurs by displaying a convex shape. The opposite case (i.e., $a < 1.0$) generates a concave shape in the transition between pure-spatial and pure-temporal covariance, as seen in Figure 5g. Additionally, due to the function

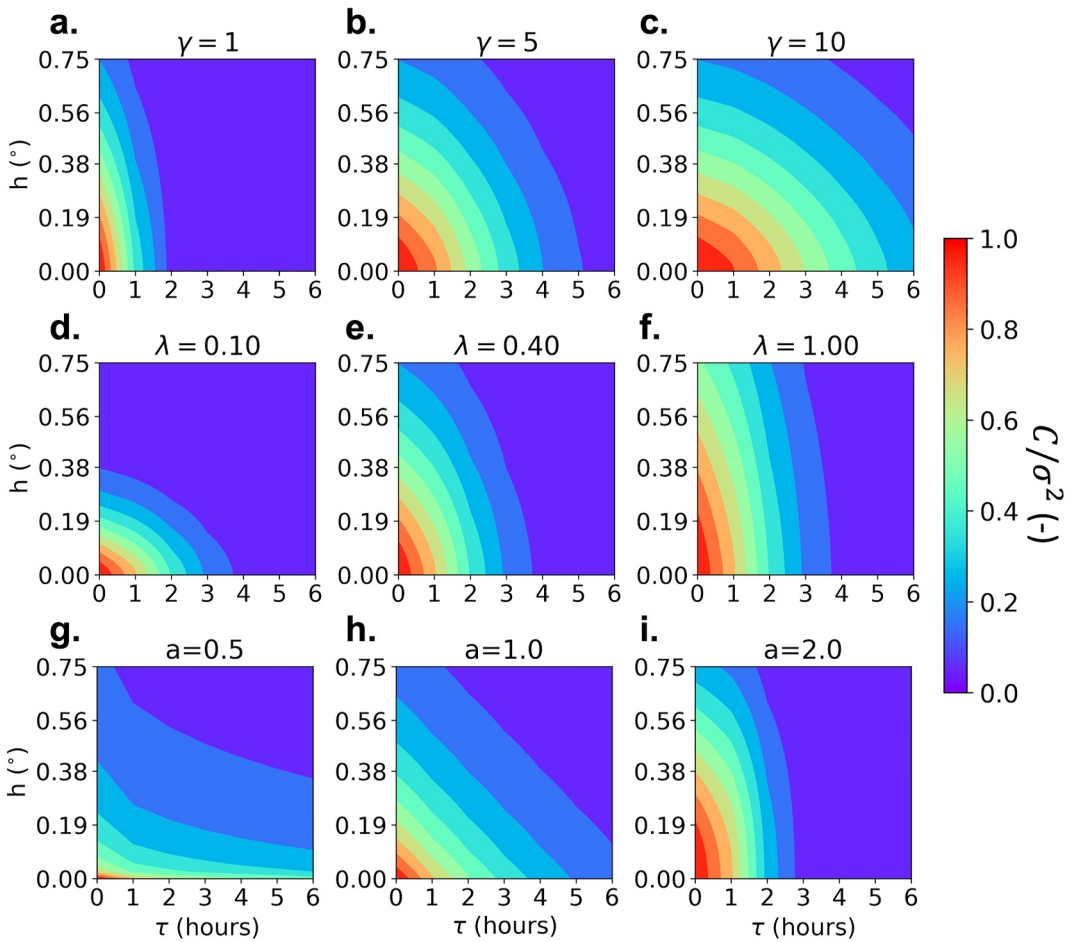


Figure 5. Parametric spatio-temporal covariance function obtained by individually increasing the values of the three main model parameters: (a–c) varying γ with $\lambda = 0.4$ and $a = 1.5$; (d–f) varying λ with $\gamma = 3$ and $a = 1.5$; and (g–i) varying a with $\lambda = 0.4$ and $\gamma = 3$.

structure, the modeled memory and spatial coherence emulated by the parametric model are also directly influenced by the magnitude of the spatio-temporal interaction exponent, a . In each dimension, the presence of the exponent determines a stretched exponential shape for the correlation function, which encompasses longer tails ($a < 1.0$) or shorter tails ($a > 1.0$) compared to a simple exponential, while retaining a characteristic scale (Laherrère & Sornette, 1998).

Additionally, modified forms of the spatial and temporal characteristic length scales can be derived to obtain an approximation unaffected by the spatio-temporal interaction exponent and identify the individual effects of space and time on the joint spatio-temporal dynamics. Tests on the data have shown that the modified forms of the characteristic length scales correspond to coordinates where the covariance is reduced to $\sim 50\%$ of its maximum value at $h = 0$ km and $\tau = 0$ hr. These modified forms are estimated as the fitted characteristic length scales operated by the fitted spatio-temporal interaction exponent, as displayed in Equations 4 and 5.

$$\gamma' = \sqrt[3]{\gamma} \quad (4)$$

$$\lambda' = \sqrt[3]{\lambda} \quad (5)$$

To fit the ESTCFs to the parametric model, non-linear least squares regression is used. The function is set up to use the Trust Region Reflective method, TRF, to perform the minimization. The TRF method is particularly suitable for large sparse problems with bounds, and it is generally robust. Based on an analysis of the selected function, the bounds for the parameters to be fitted are defined as $0 < \gamma \leq 100$, $0 < \lambda \leq 10$, and $0.5 < a \leq 3$.

2.2.6. Clustering Analysis

Once the parametric model is fitted to the ESTCFs, an unsupervised clustering algorithm determines subdomains with relatively homogeneous parameter values. Such spatial clustering has been used to map zones that represent co-varied features in a tractable manner (e.g., Devadoss et al., 2020; Wainwright et al., 2022). The commonly used k-means method is selected as a clustering algorithm. The features used to perform the clustering are the fitted spatio-temporal characteristic length scales and interaction exponent, as well as the spatio-temporal variance computed directly from the LST data. Each feature is normalized by its minimum and maximum values before performing the clustering. The dissimilarity between two data points is determined based on the Euclidean distance. To determine the appropriate number of clusters to use, the elbow method is adopted. In the elbow method, k-means clustering is performed on the data set for a range of k values (i.e., number of clusters). Then, for each k , the method computes an average score for all clusters. By default, the distortion score is computed. The distortion scores the sum of square distances from each point to its assigned center in the clustering. Once this metric for k is plotted, it is possible to visually determine the best value for the number of clusters, as the k where the inflection point of the curve occurs. Using the obtained number of clusters, k-means is applied, and the resulting clusters are mapped out and analyzed in terms of their characteristic spatio-temporal covariance function (CSTCF), which for each cluster is computed using the parametric model with the mean value of all the sub-domains contained within the same cluster.

3. Results

3.1. ESTCF Over CONUS

The summer daytime ESTCFs over CONUS were computed using all the available LST observations according to the procedure described in Sections 2.2.1 and 2.2.2. The obtained ESTCFs for seven locations with various landscape features are presented in Figure 6. The figure shows the site-specificity of the obtained ESTCFs. As expected, the spatio-temporal variance of LST (i.e., the maximum value of the color bar) was higher for mountainous areas (i.e., Colorado and Lake Tahoe, Figures 6b and 6c), and for coastal regions, including lake coastlines (i.e., New York City and Lake Michigan, Figures 6f and 6g), due to contrasting landscape features such as topography and material thermal properties. The observed variance values for flat areas were relatively low, with values around 3 K² for the Louisiana, Atlanta, and North Dakota domains (Figures 6d, 6e, and 6h).

It was observed that the contrast between land cover types, particularly water versus land, increased the space-time interaction by producing a convex transition between space and time in the ESTCFs. The same convex transition was observed for mountainous regions (Figures 6b and 6c). Additionally, domains containing features such as rivers, cities, and small lakes (Figures 6d, 6e, and 6h), which had generally homogeneous landscapes except for the small-scale features (i.e., in the order of 10–30 km), displayed a relatively sharp decay in their spatial coherence. Domains displaying large-scale heterogeneity, driven by topography or contrasting land cover (especially land vs. water), showed larger spatial coherences (see Figures 6b, 6c, 6f, 6g).

Regarding the temporal memory of the ESTCFs in the analyzed domains, it was observed that the presence of large-scale landscape features, such as bodies of water and topographic gradients, increased the temporal memory of the ESTCF. The domains with the longer memory of summer daytime LST were the ones located in Colorado (~5 hr, Figure 6c), California (~4 hr, Figure 6b), and New York City (~2.5 hr, Figure 6f). Smaller memory values, in the order of 1 hr, were detected for all the other domains.

3.2. Sensitivity to Sampling

As described in Section 2.2.3, the sensitivity of the ESTCFs was tested with respect to the spatio-temporal sampling used. This procedure was performed for the five scenarios presented in Table 1 and the seven locations introduced in Figure 6a. Figure 7 summarizes the results of this sensitivity evaluation.

Figure 7 shows how the overall structures of the baseline-ESTCFs (i.e., first column shapes) are preserved for varying spatio-temporal sampling scenarios. In general, the spatio-temporal dynamics observed for the domains does not show major variations due to differential sampling, a finding backed up by relatively low values of RMSE and mBIAS. This finding points at the relative robustness of the ESTCF method to the sampling. However, the temporal scales of variation (i.e., temporal lag associated with maximum covariance values) does show to be influenced by the sampling, particularly in the New York City and Michigan domains (Figures 7e and 7f). This

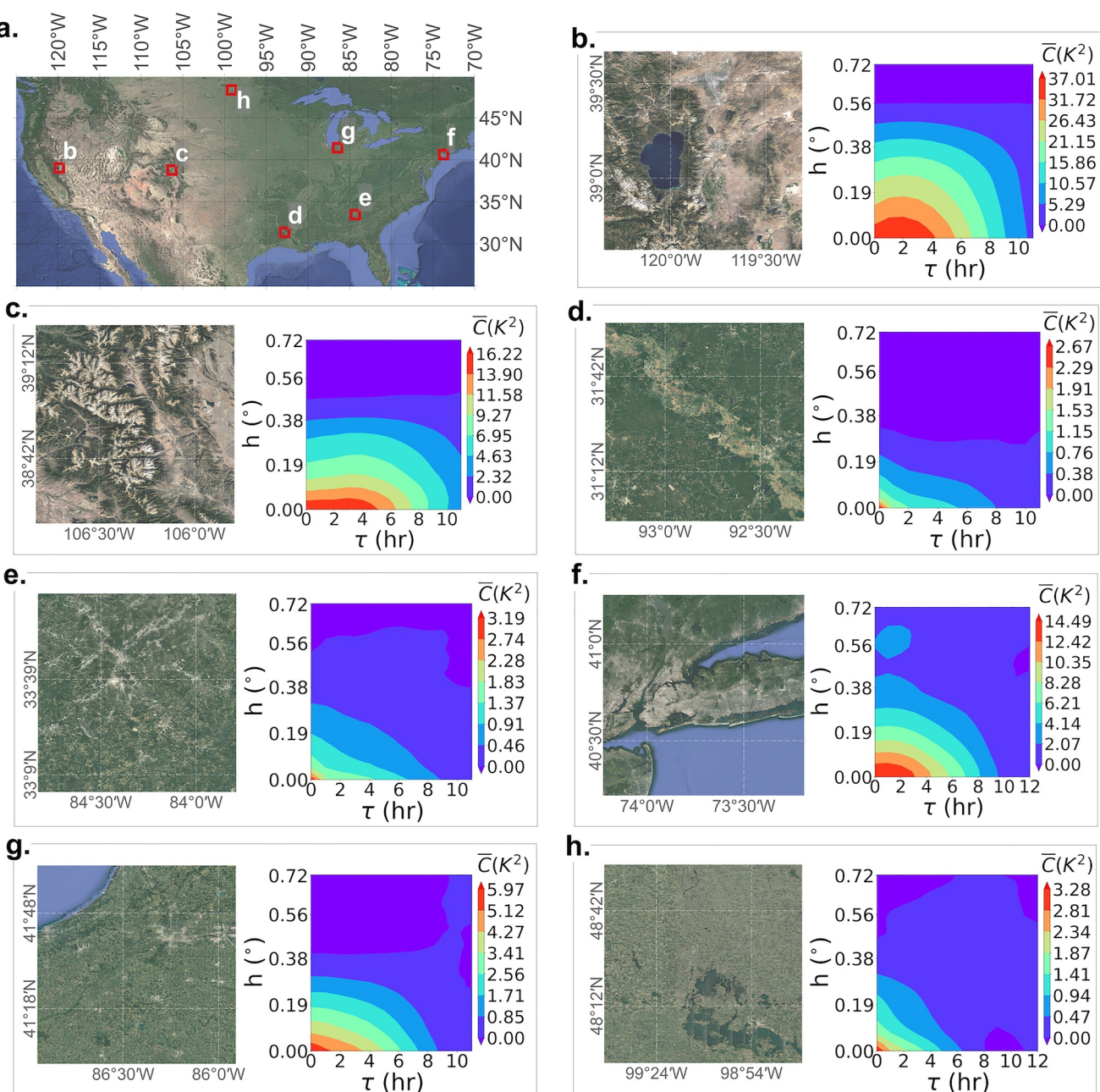


Figure 6. Zoomed-in satellite visible imagery with coordinates for seven $1.0^\circ \times 1.0^\circ$ domains over CONUS. The obtained summer daytime land surface temperature ESTCFs for each domain are also presented. (a) Location of the seven domains within CONUS; visible satellite imagery of the landscape and computed empirical spatio-temporal covariance function for (b) the Lake Tahoe area, California-Nevada border; (c) the Mount Mitchell area, Colorado; (d) Mississippi River, Louisiana; (e) Atlanta, Georgia; (f) New York City; (g) Lake Michigan shore, Indiana-Michigan border; (h) Leeds county, North Dakota.

effect is explained by the reduced availability of spatio-temporal observations (scenario 2) driven by the harsher centrality and missing value thresholds for the New York city case. In the Michigan case, on the other hand, the major changes in the temporal scale seem to be induced by the reduction in the time period used for the analysis (scenario 4). In this case, the no inclusion of observations for the years 2021 and 2022 increased the overall difference with respect to the baseline scenario. This temporal-sampling-dependence of the resulting ESTCF can also be observed, in a smaller proportion, for the Louisiana, Atlanta, and North Dakota domains, with increased values of the RMSE and mBIAS.

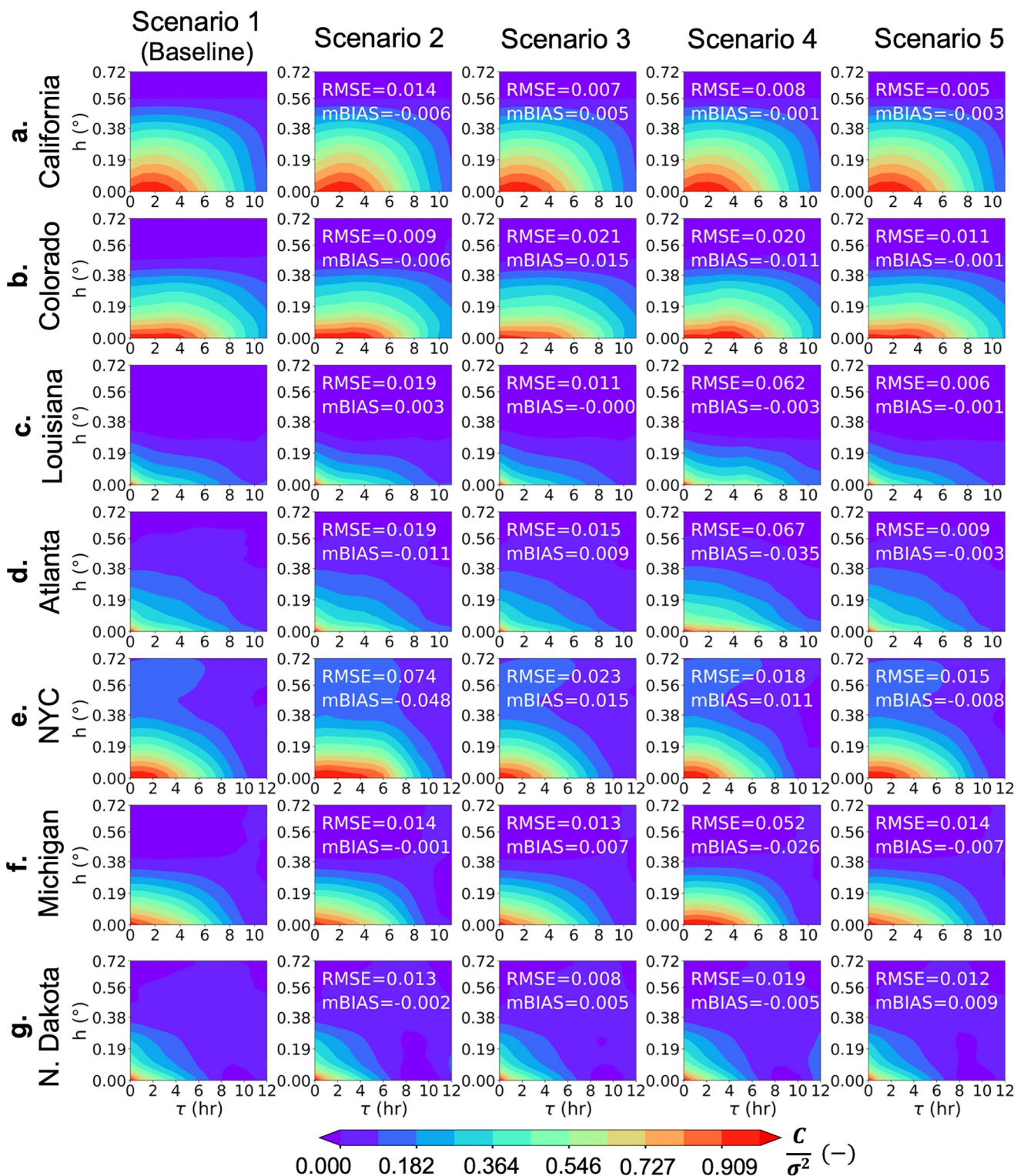


Figure 7. Results of sensitivity to sampling on seven domains over CONUS. Each column represents a sampling scenario as described in Table 1. Each row represents the domain, corresponding to the ones presented in Figure 5a: (a) Lake Tahoe area, California-Nevada border; (b) Mount Mitchell area, Colorado; (c) Mississippi River, Louisiana; (d) Atlanta, Georgia; (e) New York City; (f) Lake Michigan shore, Indiana-Michigan border; (g) Leeds county, North Dakota.

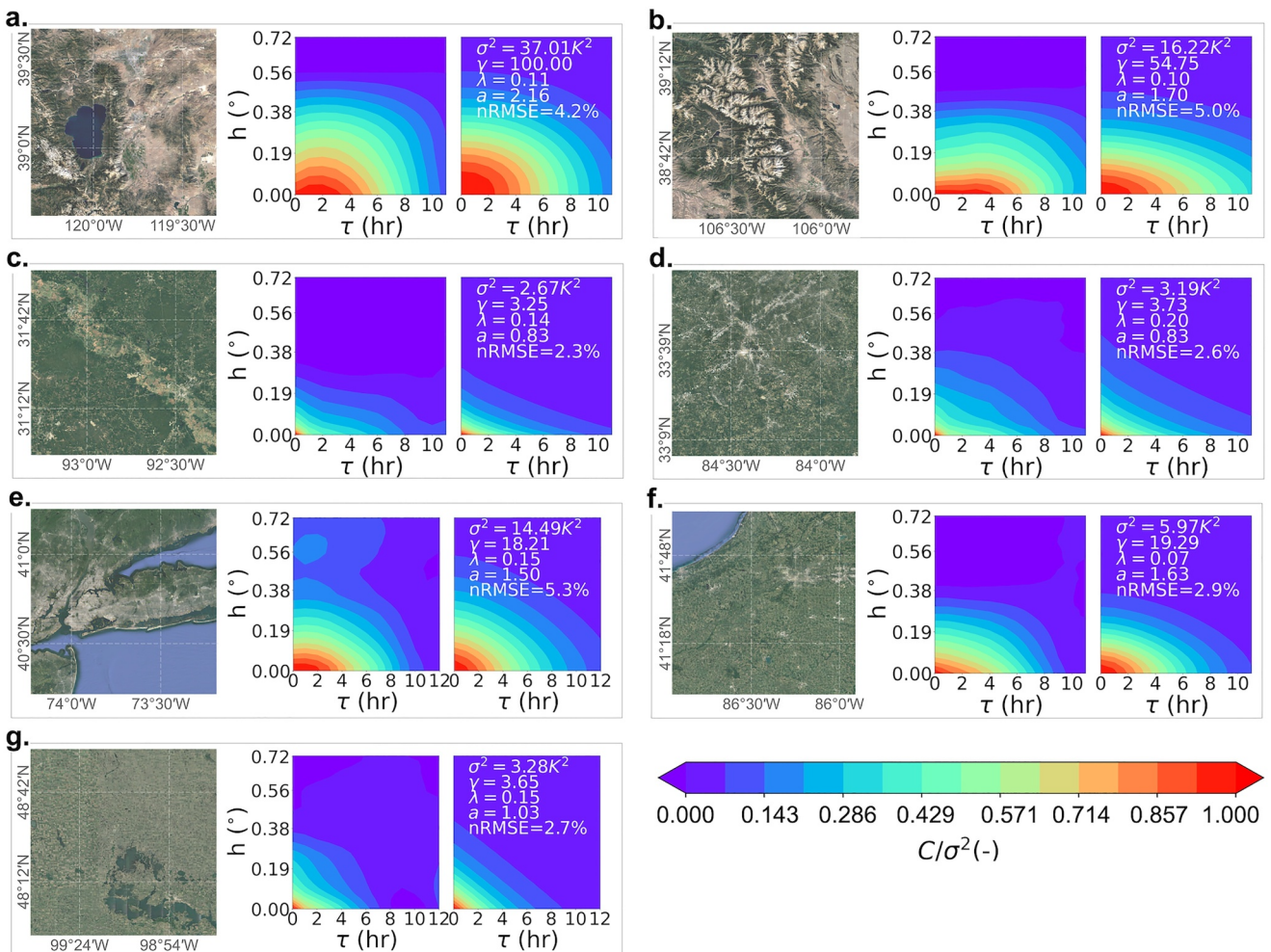


Figure 8. Zoomed-in satellite visible imagery with coordinates for the seven $1.0^\circ \times 1.0^\circ$ domains over CONUS. The obtained summer daytime land surface temperature ESTCFs for each domain and the fitted spatio-temporal covariance function parametric model are presented. The plots for the fitted cases include the obtained set of parameters and the normalized root mean square error for the fit. Visible satellite imagery of the landscape, computed empirical spatio-temporal covariance function, and fitted spatio-temporal covariance function parametric model for (a) the Lake Tahoe area, California-Nevada border; (b) the Mount Mitchell area, Colorado; (c) Mississippi River, Louisiana; (d) Atlanta, Georgia; (e) New York City; (f) Lake Michigan shore, Indiana-Michigan border; (g) Leeds county, North Dakota.

3.3. Spatio-Temporal Covariance Function: Parametric Model Over CONUS

Once the ESTCFs were computed for CONUS, the selected parametric model for the spatio-temporal covariance function was fitted to them, as described in Sections 2.2.4 and 2.2.5. The obtained parametric fits for the seven domains analyzed in Figure 6 are presented in Figure 8. For the locations of the domains over CONUS, the reader is referred to Figure 6a.

Figure 8 shows the performance of the selected parametric model in reproducing the observed ESTCFs. The Figure displays zoomed-in satellite imagery for each domain, the ESTCFs computed from the LST observations, the obtained fit, the set of parameters corresponding to that fit, and the normalized root mean square error (nRMSE) as a performance metric. Visual inspection showed that, in general, the parametric model performed well for the selected locations, particularly for the higher covariance values on the bottom left part of the spatio-temporal domains, $0.7 \leq C/\sigma^2 \leq 1.0$. This was expected, as these values played a more critical role in the normal least squares minimization algorithm used in the fit. The obtained nRMSE values confirmed the results derived from the visual inspection. Higher nRMSE values were observed for domains with larger spatio-temporal variance values (i.e., mountainous domains and coastal domains; Figures 8a, 8b, and 8e). This behavior can be explained by the fact that the selected model was overly simplistic to represent the complex space-time interactions that could emerge in some regions.

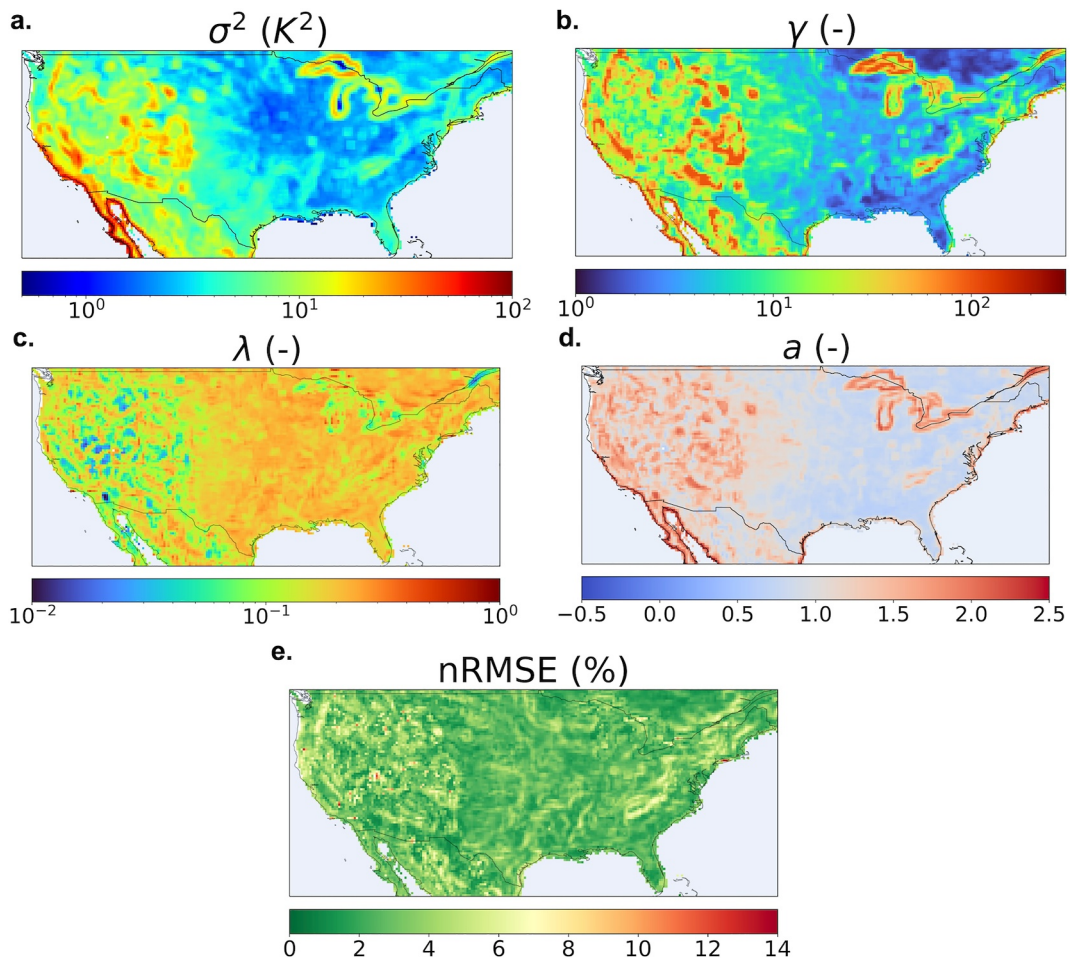


Figure 9. Maps of results for the parametric spatio-temporal covariance function fit for land-containing domains. Each pixel represents the central $0.25^\circ \times 0.25^\circ$ for each $1.0^\circ \times 1.0^\circ$ analyzed domain. (a) Computed spatio-temporal variance, (b) fitted temporal characteristic length-scale, (c) fitted spatial characteristic length-scale, (d) fitted spatio-temporal interaction exponent, and (e) normalized root mean square error for the parametric fit.

Regarding the magnitude of the obtained parameters, it was clear that domains where interactions between land and water existed (Figures 8e and 8f) and where significant topographic gradients were present (Figures 8a and 8b) displayed higher values of the temporal characteristic length-scale, γ , and values of the spatio-temporal interaction exponent, a , over 1. For the remaining domains (Figures 8c, 8d, and 8g), the spatial characteristic length-scale, λ , seemed to play a more critical role in reproducing the ESTCF, with relatively high values. Additionally, for these cases, the spatio-temporal interaction exponent, a , kept values slightly under or over 1.0, indicating an almost linear spatio-temporal interaction.

The fit to the parametric spatio-temporal covariance function model was performed for every $1.0^\circ \times 1.0^\circ$ domain under analysis with at least 2/3 of its area over land. Figure 9 presents the integrated results for this procedure as maps. Each pixel represents the central $0.25^\circ \times 0.25^\circ$ for each $1.0^\circ \times 1.0^\circ$ analyzed domain. Maps for the fitted spatio-temporal characteristic length scales, γ and λ , are presented (Figures 9b and 9c), as well as for the fitted spatio-temporal interaction exponent, a , (Figure 9d) the computed spatio-temporal variance, σ^2 , (Figure 9a) and the nRMSE obtained for the fit (Figure 9e). It is worth mentioning that the ESTCFs presented in Figures 6 and 8 did not share the same time lag axis limits due to the location-dependent day lengths. However, the temporal lag axis was standardized for the CONUS-wide fit, $0 \leq \tau \leq 8$ hr. The results reveal:

1. Spatio-temporal variance (Figure 9a): A West to East decreasing gradient of variance was observed, showing agreement with the long-term precipitation climatology for the area. Additionally, the obtained gradient was also consistent with the Köppen-Geiger climate classification system for CONUS, with drier climates

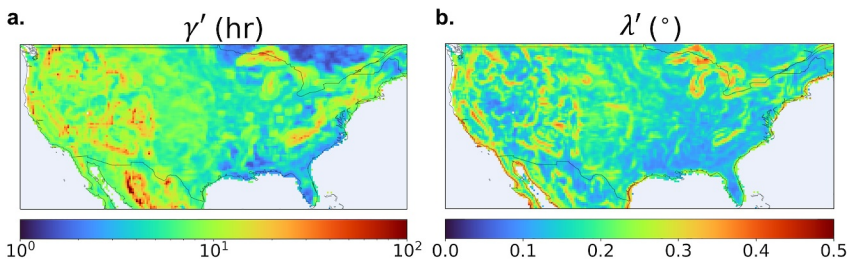


Figure 10. Maps of results for the modified forms of the spatio-temporal characteristic length scales for land-containing domains. Each pixel represents the central $0.25^{\circ} \times 0.25^{\circ}$ for each $1.0^{\circ} \times 1.0^{\circ}$ analyzed domain. (a) Modified temporal characteristic length-scale, (b) modified spatial characteristic length-scale.

displaying a larger LST variability with a lower influence of surface SMC. As expected, higher variance values were observed in regions with significant topographic gradients, coastlines, urban areas, particularly in the Midwest and the Mississippi River delta area in Louisiana. Coastal areas of the Atlantic and Pacific showed clear differences, with the Pacific coast displaying larger variance values due to a sharper contrast in temperature between land and water. The lowest values were located in flat areas in the central and eastern regions of CONUS.

2. Temporal characteristic length-scale (Figure 9b): The observations derived from Figure 7 were confirmed in this case with increased values of γ in mountain areas and coastal regions, particularly in the Sierra Nevada, Rocky Mountains, Coastal ranges, Appalachians, California Gulf, Northeast coastlines and Great Lakes shorelines. Urban areas in the Midwest, South, and Northeast also showed elevated values in comparison to their surroundings.
3. Spatial characteristic length-scale (Figure 9c): An east-to-west decreasing gradient for this parameter was observed. Higher values were identified for flat areas of the Midwest. Unlike the temporal characteristic length scale, urban sites, coastlines, and mountain ranges displayed reduced values, probably due to a heavy influence of the spatio-temporal interaction exponent.
4. Spatio-temporal characteristic length-scale (Figure 9d): The patterns observed here resemble the ones for the spatio-temporal variance (Figure 9a). Concave spatio-temporal interactions ($a < 1$) were found in flat areas of the South, non-coastal areas of the Midwest, and non-urban portions of the Northeast. Linear relationships between space and time ($a \approx 1$) were identified for urban areas of the Midwest and South, as well as in relatively homogeneous domains in the West. In general, domains containing coastlines and significant topographic gradients consistently displayed a convex spatio-temporal interaction ($a \geq 1$).
5. nRMSE (Figure 9e): The model struggled to thoroughly capture the observed dynamics in the Appalachians, Sierra Nevada, Rocky Mountains, Coastal ranges, and some urban areas of the Midwest and Northeast. However, due to the general performance, it was concluded that the selected parametric model represented the spatio-temporal dynamics of LST in a relatively accurate way, with a CONUS-wide mean nRMSE of $\sim 3\%$.

Alternative forms of the length scales were derived to obtain an approximation unaffected by the spatio-temporal interaction exponent and identify the individual effects of space and time on the joint spatio-temporal dynamics. These forms were estimated as the fitted characteristic length scales operated by the fitted spatio-temporal interaction exponent (as described in Section 2.2.5). Another goal of this procedure was to identify locations where the spatial characteristic length-scale displayed patterns that could not be placed directly from Figure 9. Figure 10 shows the maps of the alternative forms of the spatio-temporal characteristic length scales with units. In general, the modified temporal characteristic length-scale (Figure 10a) displayed some of the same patterns identified using Figure 9b: increased values in mountainous areas and urban zones in the Midwest, South, and Northeast with elevated values compared to their surroundings. For mountainous regions, the magnitude of the modified temporal scale (i.e., memory) was in the range of 20–60 hr (i.e., one day to 2.5 days). For the urban areas cases, the obtained memory was on the order of 10 hr. However, unlike Figure 9b, Figure 10a showed that the contrast between land-only domains and coastal domains, particularly in the California Gulf, the Great Lakes shorelines, and the Northeast coastline, was not as high for the modified temporal characteristic length-scale, with memories slightly below 10 hr. This implies that the increased values of γ in these locations were caused by an elevated space-time interaction exponent rather than by a time-only effect. On the other hand, the modified spatial characteristic length-scale (Figure 10b) displayed increased values in domains with persistent landscape features,

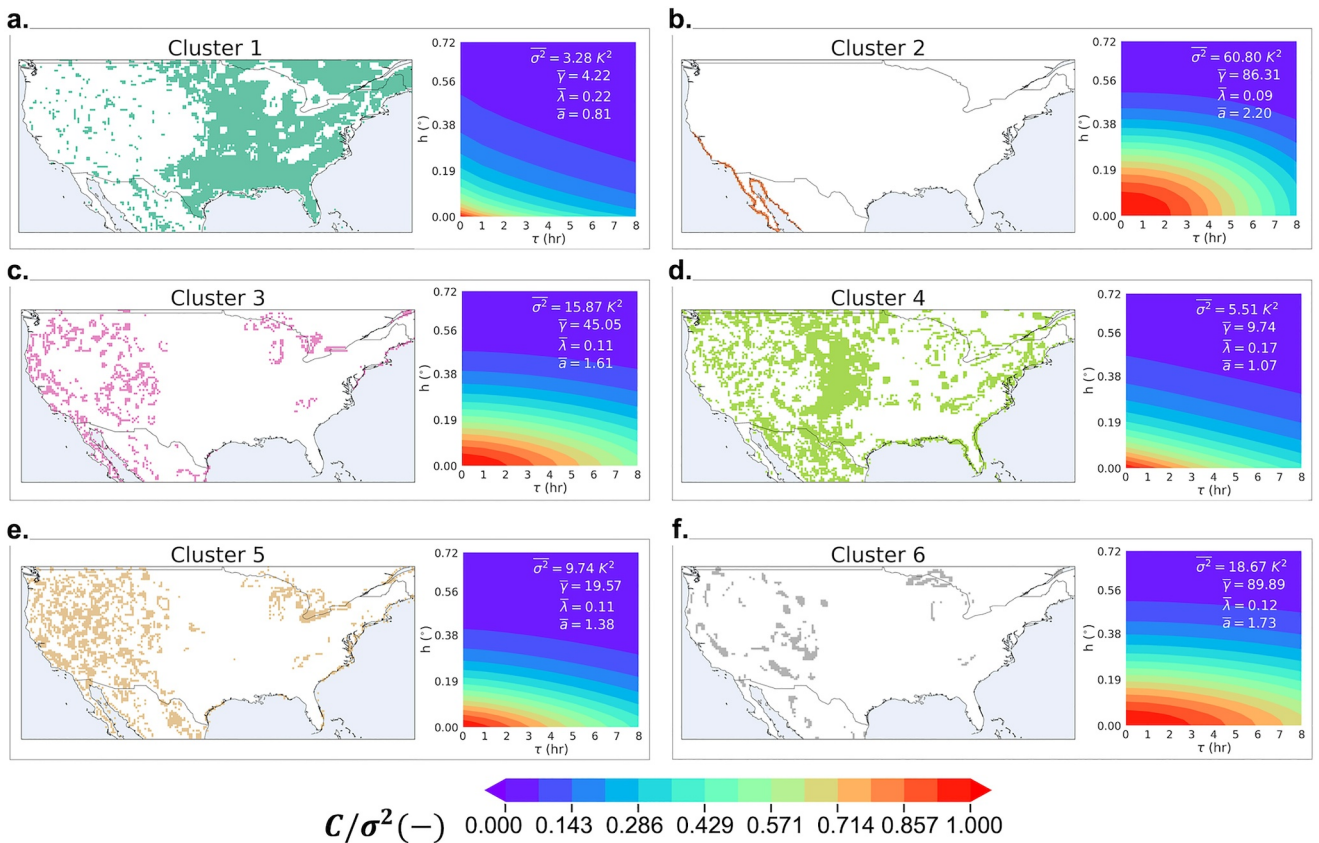


Figure 11. Individual spatial mapping of the clusters over CONUS, next to the corresponding characteristic spatio-temporal covariance function obtained as the mean cluster value of the parameters for (a) cluster 1, (b) cluster 2, (c) cluster 3, (d) cluster 4, (e) cluster 5, and (f) cluster 6.

including coastlines and mountain ranges, a pattern expected but not observed on the original spatial characteristic length-scale map (Figure 9c). In this sense, for these locations, the spatio-temporal interaction parameter reduced the influence of the space-only characteristic length-scale, probably due to the magnitude of the distances (below 1°).

3.4. Clustering Analysis and Related Physical Covariates

With all the parameter values from the model fit, an unsupervised clustering algorithm (i.e., k -means) was used to identify homogeneous zones. The number of clusters to be used (i.e., $k = 6$) was determined using the elbow method based on the distortion score.

Figure 11 presents the spatial mapping of the clusters over CONUS, as well as the parametric representation of the spatio-temporal covariance function obtained from the mean cluster value of the parameters (i.e., the mean value of the parameter values for all the domains contained within the same cluster) or CSTCF. The first observation derived from Figure 11 is the variance discrimination between groups. In general, locations with higher variances, $\bar{\sigma}^2$, (i.e., Pacific coast and Gulf of California, higher elevations of Rockies, Sierra, Coastal ranges and Appalachians, and shorelines of Lakes Superior, Michigan, Huron, and Ontario) were grouped by the clustering procedure in Cluster 2, Cluster 6, and Cluster 3, respectively (Figures 11b, 11f, and 11c). Due to the topographic and material contrast within those high variance domains, the obtained shape for the CSTCF was predominately convex with mean exponent values \bar{a} over one, particularly in the Cluster 2 case. That was also the case for the mean characteristic temporal length-scale, $\bar{\gamma}$, with the highest values associated with the larger variance clusters. Due to the previously discussed influence of the spatio-temporal interaction exponent, the mean characteristic spatial length-scale results were less clear. As for the lower variance clusters, Cluster 1, Cluster 4, and Cluster 5 (Figures 11a, 11d, and 11e, respectively), each exhibited distinctive characteristics. Besides presenting the lowest $\bar{\sigma}^2$ values, Cluster 1 displayed low values of $\bar{\gamma}$ and \bar{a} (i.e., concave shape). Cluster 4 featured the second lowest

Table 3

Mean Variance and Alternative Forms of Temporal and Spatial Length Scales per Cluster

Cluster ID	σ^2 (K ²)	γ' (hr)	λ' (°)
1	3.28	5.92	0.15
2	60.80	7.59	0.34
3	15.87	10.65	0.25
4	5.51	8.39	0.19
5	9.74	8.63	0.20
6	18.67	13.47	0.29

Note. The colors indicate the scale of variation of each column (green for the lowest values to red for the highest values).

variance with an almost linear space-time interaction exponent, \bar{a} , and relatively low $\bar{\gamma}$. Finally, Cluster 5 constituted a transitional group with the third lowest variance but relatively high values of both \bar{a} and $\bar{\gamma}$.

To obtain an approximation unaffected by the spatio-temporal interaction exponent and identify the individual effects of space and time on the joint spatio-temporal dynamics, Table 3 displays the alternative forms of the length scales for each CSTCF; the variance is also presented. The table shows how Clusters 6 and 2 displayed the overall higher spatio-temporal dynamics with the highest values of variance and spatial length-scale (Cluster 2) and highest temporal length-scale and second highest spatial length-scale (Cluster 6). Cluster 3 is also worth mentioning as it showed relatively high values of all the parameters. Clusters 4 and 5 showed relatively low variance and spatial length-scale values but significant memory in time (~ 8 hr). Finally, Cluster 1 displayed the least dynamic behavior with the lowest variance value, spatial length-scale, and temporal length-scale.

Figure 12 presents the analysis of the physical features of the domains that could be relevant in determining the obtained clustering of spatio-temporal parameters. Mean values of spatial standard deviation for the domains included in each cluster are presented for each tested physical feature. The mean standard deviations for all the domains over CONUS are also presented (dotted lines). The Figure shows:

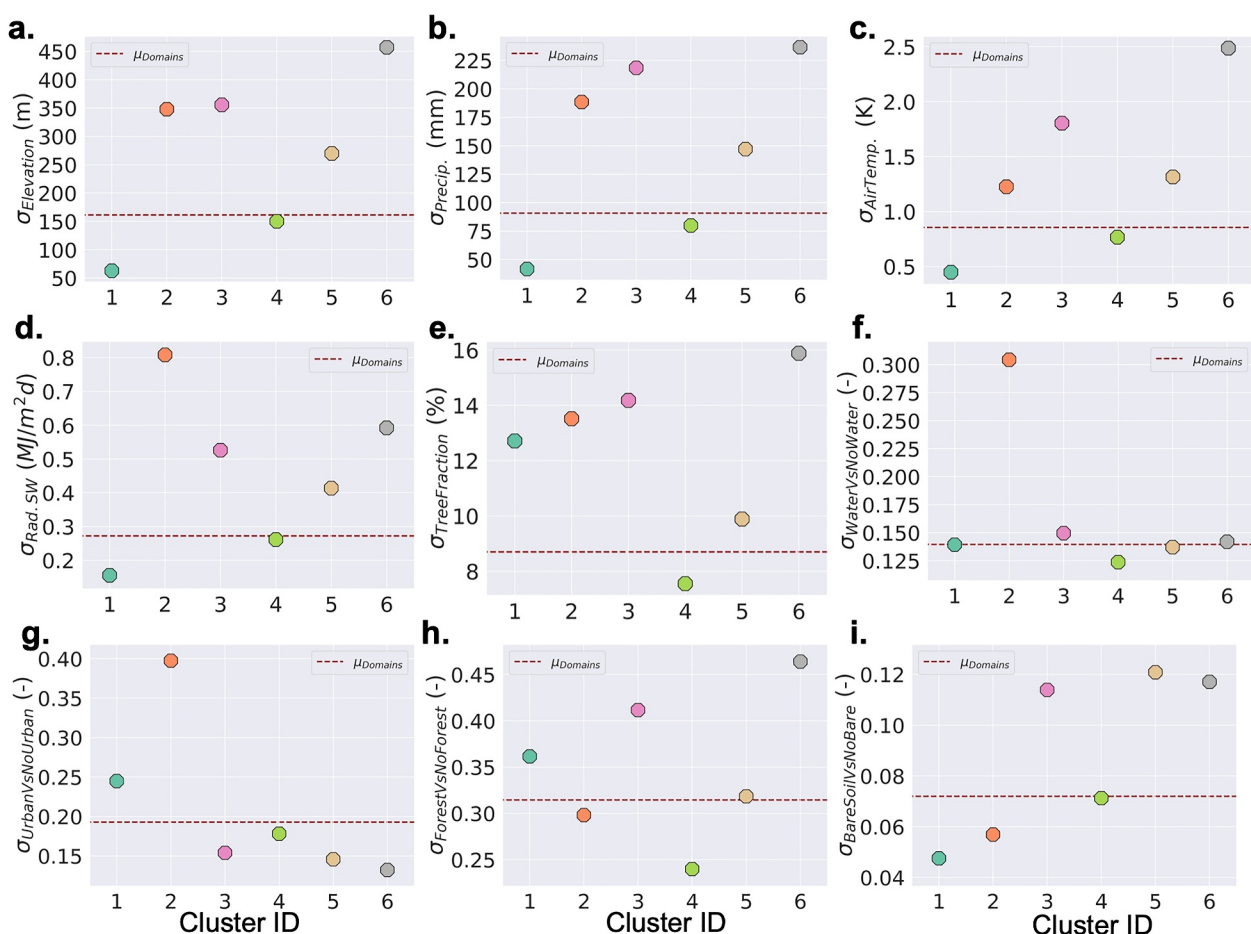


Figure 12. Mean cluster values of standard deviations of physical features under analysis. The red dotted lines indicate the CONUS-wide mean value for all domains. (a) Elevation standard deviation, (b) precipitation climatology, (c) air temperature climatology, (d) shortwave downward solar radiation, (e) tree cover fraction, (f) water versus no water, (g) urban versus no urban, (h) forest versus no forest, and (i) bare soil versus no bare soil.

- **Cluster 1 - LV-LTS-LLS-LSTI** (i.e., lowest variance, alternative temporal length-scale, alternative spatial length-scale, and spatio-temporal interaction exponent): The domains contained within this cluster showed reduced variance in elevation and its associated meteorological features (i.e., precipitation, air temperature, and shortwave downward radiation). Although some variability in tree fraction and urban and forest coverage was observed, these features were not large enough to increase the cluster's LST variance, memory (i.e., alternative temporal length-scale), and spatial coherence (i.e., alternative spatial length-scale). As for the spatio-temporal interaction exponent, the cluster displayed a relatively linear relation between space and time, probably due to the dampening influence of the cluster's relatively dense vegetation in the surface temperature dynamics.
- **Cluster 2 - HV-LTS-HSS-HSTI** (i.e., highest variance, second lowest alternative temporal length-scale, highest spatial length-scale, and highest spatio-temporal interaction exponent): In contrast to Cluster 1, the domains contained within Cluster 2 showed increased variability in elevation, precipitation, shortwave downward radiation, and water and urban coverages. The increased variability in multiple physical features, and in particular the contrast in thermal inertia between the Pacific Ocean water and the arid land in the Gulf of California, increased the overall variance of LST as well as the obtained coherence in space for the patterns in the cluster (i.e., the characteristic spatial scale of the water patches, $\sim 0.3^\circ$, agrees with the mean standard deviation of the cluster, ~ 0.34). Finally, the spatio-temporal interaction displayed a strong convex transition associated with coastal domains (see Figures 6f and 6g). This shape might be related to the contrast in thermal properties between land and water, determining the spatio-temporal dynamics in these domains.
- **Clusters 3 and 6 - HV-HTS-LSS-HSTI** (i.e., second highest variances, largest alternative temporal length-scales, second highest alternative spatial length-scales, and second highest spatio-temporal interaction exponents): The domains contained within Clusters 3 and 6 displayed the highest variabilities in multiple physical features such as elevation, precipitation, air temperature, tree cover fraction and forest and bare soil coverages. This significant variability in multiple physical features increased the overall variance of LST and the obtained memory in time for the patterns in these clusters (with values between ~ 10.5 and ~ 13 hr, Clusters 3 and 6 showed the highest memory). It is hypothesized that the high memory responds to the static topographic effect: high lands are consistently colder than lowlands, and the diurnal cycle (~ 12 hr) is the main temporal factor causing variations in the surface temperatures domain-wise. As for the spatial length scales, both clusters showed relatively high values, with scales ranging from 1/4 to 1/3 of the domain size (i.e., 0.25° – 0.3°). Again, this spatial coherence might respond to a topographic effect. Finally, unlike Cluster 2, Clusters 3 and 6 did not show the highest values of spatio-temporal interaction exponent. Even though the obtained spatio-temporal transition is still convex, the material contrast in the domains is not as significant as that observed between water and land for Cluster 2. However, especially for domains containing coastlines for bodies of water smaller than the ocean (e.g., Great Lakes and Lake Tahoe) or coastal domains with weaker temperature gradients between land and water (e.g., Northeast Atlantic coast), it appears that lower spatio-temporal interaction exponents than the ones needed for Cluster 2, might be enough to represent the transition.
- **Clusters 4 and 5 - LV-ITS-LSS-LSTI** (i.e., second lowest variances, intermediate alternative temporal length-scales, second lowest alternative spatial length-scales, and second lowest spatio-temporal interaction exponents): Clusters 4 and 5 were mainly characterized by relatively low variability in most of the physical features under analysis, except high variability in bare soil cover for Cluster 5. This lack of properties variation led to a relatively low spatio-temporal variance, spatial and temporal length scales, and spatio-temporal interaction exponents. However, for Cluster 5, the combined effect of topography, some coastal domains in the Great Lakes and Northeast Atlantic coast, along with the increased variability between bare and vegetated soil, produced a slightly increased spatio-temporal interaction exponent (i.e., relatively convex transition between space and time) and higher spatio-temporal variance. Interestingly, coastal domains to the west of Florida, contained in Cluster 4, did not increase the overall exponent (probably due to the smoother temperature contrast between water and land in that zone of the Atlantic).

4. Discussion

4.1. General Implications and Specific Application Findings

4.1.1. General Implications

This study introduced the ESTCF to evaluate the spatial coherence and temporal memory of remotely sensed spatio-temporal fields. The main aim was to uncover significant spatio-temporal patterns within the observed

processes in the Soil-Vegetation-Atmosphere System (SVAS). The ESTCF was easily obtained from gridded observations and proved flexible enough to deal with missing data, and varying spatio-temporal aggregation scales. Additionally, the ESTCF displayed the ability to characterize spatio-temporal regimes based on features of the fields such as spatio-temporal variance, spatial coherence structure, temporal memory, and space-time interactions. Overall, the proposed parametric model of the covariance function accurately emulated the empirical data while simultaneously summarizing the dynamics within the ESTCFs. The simplified features were then used to identify areas with homogeneous spatio-temporal dynamics, successfully classifying domains based on their main spatio-temporal features.

4.1.2. Application to LST: Implications for Land-Atmosphere Interactions

Regarding the application of the proposed methods to the LST fields, the use of the clustering procedure allowed the identification of zones with higher spatio-temporal dynamics in coastal domains of the Gulf of California and the South Pacific region and domains containing the highest elevations of mountainous areas (i.e., the Sierra Nevada, Rockies, Coastal Ranges, Appalachian Mountains) as well as the coastal areas surrounding the largest lakes in the Great Lakes region. These locations coincided with those reported in the literature where thermally driven circulations develop including urban boundaries (Q. Li et al., 2021; Y. Wang et al., 2017), mountain topography (J. S. Wagner et al., 2015), and land-sea and land-lake breezes (Crosman & Horel, 2010; Y. Wang et al., 2017); Gulf of California sea breezes, Great Lakes lake breezes, Rocky Mountains mountain-valley circulations, and Appalachians low level moisture convergence (Banta, 1995; Douglas, 1995; Keen & Lyons, 1978; Kindle et al., 2002; Lyons, 1972; Ohashi & Kida, 2002; Sills et al., 2011; Turnipseed et al., 2004; Whiteman et al., 2009; Wilson & Barros, 2015; Zardi & Whiteman, 2013; Zuidema et al., 2007). The main drivers of the increased spatio-temporal variability in these locations were the temporal characteristic length-scale and the spatio-temporal interaction component. These findings reinforce the essential influence of the memory of the spatio-temporal structure of the fields in the presumed potential of land-atmosphere coupling development.

While large scale studies show clear impact of land heterogeneity on convection in atmospheric simulations (Knist et al., 2020), literature specifically showing continental and global scale prevalence of heterogeneity driven flows to fully evaluate the connection between spatio-temporal structure and land-atmospheric coupling is limited. This is due in part to computational constraints in resolving these flows, which require grid resolutions nearly four times the scales of heterogeneity to resolve thermally driven circulations (Zheng et al., 2021). As such, much of the work has been limited to LES studies over specific locations. The clustering analysis presented here identifies areas of known thermally driven circulations clustered with areas where the phenomenon has not been studied, pointing to new locations where the surface thermal structure shows potential for atmospheric response and prioritizing locations for evaluation of any new model parameterizations of these flows. Ongoing work is exploring these flows and their broader atmospheric impact at the continental scale and connecting the observed spatial patterns to variations in mesoscale motions.

4.2. Limitations and Implications of Method Choices

4.2.1. Issues Regarding the ESTCF

The ESTCF was selected in this study as the tool to summarize the spatio-temporal dependence structure of remotely sensed fields of LST over CONUS. The tool was chosen as it is generally readily attainable from the available remotely sensed data, providing a relatively dense characterization of the heterogeneity degree on different spatial and temporal scales. Although this tool provides a promising path forward for a robust evaluation of the multi-scale spatio-temporal heterogeneity in large-scale observational fields, the limitations of the methodology should be considered.

1. *Sampling issues:* The accuracy of the ESTCF is highly dependent on the number of available observations for the covariance computation in each spatio-temporal distance. As mentioned in Section 2.1.1, cloud cover and atmospheric aerosols directly influence the LST retrieval processes, as they can obstruct the satellite's view of the surface, leading to spatial data gaps and reduced observations over time. In general, it is well known that cloudiness leads to cool biases in satellite-derived LST, particularly within cloudy areas (e.g., mountainous areas). Additionally, developed heterogeneity-driven circulations might lead to increased cloudiness, which

could negatively impact the quality of the available fields of observation in specific domains. Some insight into this effect was provided by the sensitivity analysis carried out in Section 3.2. Other factors affecting the retrieval of different variables (SMC, snow coverage, vegetation fraction, and material differences, among others) will undoubtedly impact the accuracy of the computed ESTCFs if different processes are analyzed. In this sense, future work should investigate further the sensitivity of the ESTCFs to the availability of observations in data-limited domains, as well as the effects of this sampling on the parameter values used for characterization purposes.

2. *Selection of a spatio-temporal covariance parametric model:* The selected structure for the covariance function parametric model was chosen as a trade-off between the number of parameters (and their physical interpretability) and an accurate representation of the data-derived ESTCFs. However, this structure represents one of many possible alternatives to model the spatio-temporal dynamics of geospatial fields. Research on geostatistics has derived many forms for covariance models, and more are expected to be developed (Bolliger et al., 2007; W. Chen et al., 2021; de Iaco, 2010; Gneiting, 2002; Ma, 2003; Schepanski et al., 2015). The selected function imposes a specific a priori structure to the spatio-temporal dependence that might not be appropriate for all domains, variables, time aggregations, or applications (e.g., not all domains or variables would benefit from a non-separable, exponential parametric model). In the results of this work, this issue was evident in the larger nRMSE values for the fits obtained for mountainous regions. Consequently, further investigations should apply the ideas exposed throughout this study to other spatio-temporal covariance parametric models in order to determine the most appropriate version of it. Non-stationary covariance structures could also be considered for specific processes as it is expected that, in some cases, the covariance structure may change in response to physical changes in the equilibrium state of the system under analysis. Finally, directional effects might also need to be considered in the computation of the ESTCFs and their fitted parametric model as the assumption of isotropy might not be appropriate for all landscapes, applications, or variables. The method can be adapted to account anisotropic effects in the fields by simply splitting the sampling and computation into directional ESTCFs (e.g., vertical, horizontal, or diagonal).
3. *Temporal and spatial resolutions and scales:* In this study, the spatial extent of the domains was set to $1^\circ \times 1^\circ$ with an hourly temporal resolution over CONUS. Although these temporal and spatial resolutions were appropriate to analyze mesoscale land-atmosphere circulations with an ESM framework in mind, applications requiring finer or coarser temporal and spatial resolutions (i.e., diurnal cycle evaluations) would most likely require the definition of a different structure for the covariance function parametric model. It is possible that the goodness of fit of analytical covariance functions may exhibit some dependence on the domain size used in the analysis. Thus, further analyses of the proposed approach over varying time windows, domain sizes, and spatio-temporal scales are also a welcome follow-up contribution. Preliminary work by the coauthors has proved the utility of the ESTCF approach in summarizing the spatio-temporal information contained within a long-term (i.e., >10 years of record length), global, remotely sensed LST gridded product (Freitas et al., 2013). However, further analyses will examine the effects of the selected moving window size, spatial offset, analyzed time period, and temporal aggregation in the obtained ESTCFs. The accuracy of the proposed parametric covariance model under these varying conditions will also be tested.
As for the temporal representativeness, the GOES-LST product is generated once an hour for every CONUS scan, with the duration of each scan being ~ 2.6 min. In this sense, even though during the ESTCF computation procedure, it is assumed that the satellite observations are representative of an entire hour, they are only short snapshots of the surface state during that time. A more comprehensive temporal representativeness would inevitably involve using the available ABI CONUS scans every 5 min. However, this presents a new challenge as the LST product is not available for that temporal scale, which would require the variable to be estimated from the available raw bands. Future research directions should look into the impact of this issue on the obtained ESTCFs.
4. *Comparison to other statistical methods for spatio-temporal analysis:* In the Introduction section, multiple statistical approaches for analyzing spatio-temporal data sets were presented. These approaches can be applied in space and/or time and have proved to be helpful in simplifying complex data sets, decomposing, and identifying relevant spatial and temporal signals, and determining critical scales of processes within the SVAS. As such, future work should compare these extensively used methods of spatio-temporal analysis to the proposed ESTCF-parametric model method introduced in this study to determine advantages and differences in the identified spatio-temporal features.

4.2.2. Remote Sensing of LST and SST

In this study, a coupled LST-SST product was employed to explore the spatio-temporal patterns of remote sensing surface temperature. However, as mentioned in Section 2.1, remote sensing retrieval of LST and SST are intrinsically different, with each of them presenting particular challenges.

Surface temperature remote sensing retrieval poses inherent challenges due to multiple factors impacting measurement accuracy and precision. Among these challenges, the intrinsic diversity of Earth's surface materials stands out. Each surface type possesses distinct thermal characteristics, emissivity values, and heat exchange mechanisms, resulting in varying thermal energy emission patterns. This diversity makes the algorithm heavily dependent on the feed surface emissivity values and land-water mask. Furthermore, the presence of atmospheric water vapor significantly affects the thermal infrared signal detected by satellites, often leading to an underestimation of actual surface temperature compared to the measured brightness temperature. The relationship between radiance and temperature is also nonlinear, rendering traditional linear models, like the single and split channel methods, less precise, particularly in hot and humid atmospheric conditions (Duffy et al., 2022). This discrepancy is amplified with increasing column water vapor, making the inclusion of water vapor data crucial for enhancing LST accuracy (Sobrino et al., 1993). However, the spatial and temporal variability of the atmospheric conditions further complicates the retrieval process, as they introduce error propagation and uncertainties into the estimates.

In this sense, remote sensing-derived surface states inevitably depend on assumptions about the overlying atmosphere and landscape features, and estimations ultimately constitute a model output. This produces a relatively high uncertainty, mainly since there is no observational "truth" at the landscape scale for comparison (Stisen et al., 2011). However, the information content present in the spatio-temporal structure of the observed satellite fields is intrinsically valuable, especially when considering the wide variety of variables of surface states and fluxes currently estimated (e.g., SMC (Chan et al., 2018; Entekhabi et al., 2010; Kerr et al., 2012; Parinussa et al., 2015; W. Wagner et al., 2013), evapotranspiration (Boschetti et al., 2019; J. B. Fisher et al., 2020; Martens et al., 2017; Running et al., 2019; Su, 2002), snow cover fraction (Painter et al., 2009; Tsai et al., 2019), and changes in water storage (Tapley et al., 2004)).

4.3. ESTCF Applications

4.3.1. Toward the Improved Representation of Land-Atmosphere Interactions in ESMs

The approach presented in this study provides more than a tool to summarize the spatio-temporal dependence structure of remotely sensed fields. We have proved that ESTCF can also be employed to estimate the characteristic length scales of heterogeneity, providing parametrizations with useful spatio-temporal information over macroscale grid cells. The method also assesses the spatial coherence and memory of the fields and allows the identification of regions with homogeneous characteristics. By identifying these locations, ESTCF can help inform parametrizations schemes for ESMs by distinguishing locations and times for which the common flux averaging methods might be insufficient to represent interactions between model components, particularly the interaction between land and atmosphere. Ultimately, the hope is that the type of approach presented through this study drives the ESM community in a direction where the representation of the subgrid-scale heterogeneity in both space and time is considered both in model development and as a model diagnostic tool.

4.3.2. Model Evaluation: Spatially Distributed Hydrological Models

Physically based spatially distributed hydrological models allow the simulation of the spatial distribution of hydrological and hydraulic processes within catchments while still providing discharge estimates for the river network. However, most spatially distributed hydrological models are still calibrated and evaluated using a goodness of fit metric describing the efficiency of the model representation of a catchment-aggregated or point-retrieved quantity, such as discharge (Zink et al., 2018). This practice generally makes the models overparametrized relative to the data available to constrain them (Stisen et al., 2011). It is widely accepted that model calibration and validation practices for these models should take directions that agree more with the spatially distributed nature of the outputs, including continuous spatial observation data (Beven, 2001). The main issue, however, is the lack of a standard set of techniques and metrics to evaluate the goodness of fit of the models' spatial predictions. Several spatial performance metrics have been developed (Ko et al., 2019; Koch et al., 2015,

2016, 2017; H. T. Li et al., 2009; Stisen et al., 2011, 2021; Xiao et al., 2022; Zink et al., 2018) and reviewed in their ability to constrain and evaluate models (Wealands et al., 2005). In general, simple global statistics operating locally (i.e., pixel-to-pixel comparison of the modeled and observed maps) are insufficient as they are susceptible to small-scale spatial displacement errors and do not consider information on patterns or spatial correlation of the data. More robust global statistical metrics such as mean bias, standard deviation, and variogram ranges are not entirely appropriate, as they are also pattern agnostic. An approach like the one presented in this study can provide a robust and compact tool to evaluate the performance of spatially distributed hydrological models while still being “pattern aware.” The model representation of spatio-temporal variables and processes such as SMC, runoff generation, infiltration, and evapotranspiration can be characterized using the ESTCF tool; then, by adding catchment-aggregated observations such as streamflow, the proposed tool provides an additional constraint to be used in the calibration stage. In addition to its flexibility in terms of spatial and temporal resolution, the proposed ESTCF method has the advantage of not being limited to square or rectangular domain shapes and being readily applicable to catchment-based hydrological models.

Nevertheless, when assessing models in relation to hydrological states or fluxes derived from remote sensing, one must acknowledge that this involves comparing models to models, with considerable uncertainty inherent in both methods. This is especially true as there is no definitive observational “truth” available for landscape-scale comparisons. Furthermore, the careful selection of suitable evaluation variables and objective functions is essential to guarantee the reliability of model assessments (Stisen et al., 2011).

4.3.3. Spatio-Temporal Characterization for Alternative Applications

This study introduces the ESTCF as a versatile and comprehensive tool to depict and characterize the spatio-temporal interdependence structure of remotely sensed fields. Even though the tool is solely applied to LST fields in this study, it is recognized that application to other spatio-temporal fields might shed light on the dynamics of processes within different compartments of the SVAS. This section explores both the remote sensing data available for other applications and systems and the processes that would benefit from the application of the ESTCF method.

- SMC: Besides the relevance of soil moisture spatio-temporal patterns in the initiation of land-atmosphere circulations (see Section 1), other essential processes, such as drought onset and evolution, infiltration, surface and subsurface runoff, and inundation dynamics, all heavily depend on the spatio-temporal structure of SMC fields. However, the main limitations of the currently available SMC remote sensing products are their long revisit times and low spatial resolution. These limiting factors reduce the current applicability of the proposed methods to all the mentioned processes. However, regional flood and drought evolution analyses on longer time scales (biweekly to monthly) are still feasible using the available data.
- Fractional vegetation cover, leaf area index, normalized difference vegetation index, and enhanced vegetation index: Spatio-temporal remotely sensed fields of vegetation-related quantities and indices contain essential information related to processes such as evapotranspiration, erosion, net primary productivity, crop productivity, agricultural droughts, and turbulent energy exchange between the land surface and the atmosphere. The temporal and spatial resolution of the currently available products would enable weekly to monthly analysis over seasonal scales and regional to continental domains.
- Evapotranspiration (ET): ET is a critical process in the hydrological cycle, linking the land surface water balance, carbon cycle, and the land surface energy balance. Remote sensing provides a method to estimate ET at regional to global scales with biweekly to weekly return rates. Spatio-temporal analysis of this variable would be primarily valuable for model evaluation and calibration purposes due to the vital role of estimated ET in model structures.
- Reanalysis of atmospheric, land, and oceanic climate variables: Global, hourly, and extended records (~1940–present) of multiple variables related to different compartments of the SVAS are included within reanalysis data sets. The wide availability of this data might allow us to analyze the impacts of climate variability and climate change on the spatio-temporal dependence structure of multiple fluxes and states in systems within the SVAS.

5. Summary and Conclusions

Several approaches have been developed to identify, summarize, and extract relevant patterns from spatio-temporal geophysical data sets. These methods can be applied in both space and time, though, in general, they

are only meant to analyze independent dimensions. In climate, environmental, and hydrological applications, there is a clear advantage in concurrently detecting spatio-temporal patterns as they offer insights into the dynamics of the processes influencing them. Among the tools developed for geostatistical analysis, the ESTCF stands out for its simplicity. Under several assumptions, the ESTCF quantifies the strength and structure of dependence between different locations and times. Once the computed, it becomes possible to select a parametric covariance model and estimate its parameters by fitting the model to the empirical function. This process allows us to gain insights into the spatio-temporal properties and interactions of the original field based on the estimated parameters.

This study introduced the ESTCF as a tool for evaluating the spatial consistency and temporal memory of remotely sensed spatio-temporal fields. It was used to identify patterns that could have significance in understanding the dynamics of processes within the Soil-Vegetation-Atmosphere System (SVAS). Additionally, the study presented a parametric covariance model to summarize the spatio-temporal structure revealed by the ESTCF. These tools were then applied to remotely sensed LST fields over CONUS. Furthermore, the study proposed a clustering approach to identify areas with homogeneous spatio-temporal dependence structures. Thus, the critical developments in this study included (a) a flexible and comprehensive tool to characterize and represent the spatio-temporal dependence structure of remotely sensed fields in the form of the ESTCF, (b) a 4-parameter covariance function model to more concisely describe the spatio-temporal patterns captured with the ESTCF, (c) a multi-dimensional clustering approach to determine areas with similar spatio-temporal dependence structures, and (d) scientifically valuable local assessments of spatial, temporal, and spatio-temporal dependence scales for LST across CONUS, based on a data-driven approach.

The ESTCF, derived from remotely sensed observations, was readily accessible and demonstrated adaptability in handling missing data, varying spatio-temporal sampling scenarios, and different temporal periods. It showcased its capacity to characterize spatio-temporal patterns using field characteristics like spatio-temporal variance, spatial coherence structure, temporal memory, and space-time interactions. The proposed parametric covariance function model was also reasonably accurate in emulating the empirical data while succinctly summarizing its dynamics. The simplified attributes were then utilized to pinpoint regions with consistent spatio-temporal patterns, effectively categorizing domains based on their primary spatio-temporal characteristics. The combined use of the clustering procedure and the suggested combined metric for spatio-temporal memory facilitated the identification of zones with increased spatio-temporal dynamics. These zones included coastal areas in the Gulf of California and the South Pacific region, and regions with high elevations, such as the Sierra Nevada, Rockies, Coastal Ranges, and Appalachian Mountains. Additionally, the method identified coastal regions surrounding the largest lakes in the Great Lakes area. These findings aligned with prior literature reports suggesting an increased likelihood of mesoscale land-atmosphere circulations in locations with those landscape features. These results, however, were specific to the selected domain size, temporal aggregation, and parametric model structure. As such, it is recognized that this is just one of the many possibilities to summarize the spatio-temporal dynamics from remotely sensed fields and that more efficient and accurate strategies might exist.

The developed approach is the first attempt to objectively analyze the complex spatio-temporal dependence structure from remotely sensed fields for analysis applications. Moving forward, the transferability of the approach should be tested under various data availability scenarios, parametric model functional forms, clustering techniques, temporal windows, domain sizes, and study areas (i.e., move to global scales). Furthermore, although subject to errors and biases, using LST remotely sensed fields might help inform land-atmosphere parametrization schemes for ESMs of the real spatio-temporal distribution of the surface fluxes. The introduced approach will also be beneficial in calibrating and evaluating process-based spatially distributed hydrological models and parametrizations for land surface models. The approach can also be easily transferred to several other available remote sensing data sources, enhancing our understanding of the spatio-temporal dynamics of processes within different compartments of the SVAS. This work represents a step toward adapting model evaluation and parametrization techniques to leverage the available high-resolution data better, accounting for the dynamic nature of land surface processes. Overall, the tools introduced here provide a path forward to formally identify and summarize the spatio-temporal patterns observed in remotely sensed fields and relate those to the footprint of more complex dynamic processes within the SVAS.

Data Availability Statement

The GOES-16 LST and SST products used in this study are freely available from NOAA's Comprehensive Large Array-Data Stewardship System (CLASS). The data that support the findings of this study, including the scripts to reproject the original data to a WSG84 projection, combine LST and SST products for the CONUS region, merge individual hourly files into weekly netCDF4 files, extract the data for $1^\circ \times 1^\circ$ domains over CONUS, compute the daytime summer ESTCF for those domains, and analyze the results (i.e., mapping and clustering) are preserved at <https://doi.org/10.5281/zenodo.8428629> (Torres-Rojas & Chaney, 2023). Table 2 references the open-access data sets used to analyze the physical features of the obtained clusters.

Acknowledgments

This study was supported by funding from NOAA Grants NA19OAR4310241 (Parameterizing the effects of sub-grid land heterogeneity on the ABL and convection: Implications for surface climate, variability, and extremes) and NA22OAR4310644 (Implications of heterogeneity-aware land-atmosphere coupling in the predictability of precipitation extremes). We also want to thank the reviewers for their informative and constructive comments and suggestions.

References

- Anderson, M. C., Kustas, W. P., Alfieri, J. G., Gao, F., Hain, C., Prueger, J. H., et al. (2012). Mapping daily evapotranspiration at Landsat spatial scales during the BEAREX' 08 field campaign. *Advances in Water Resources*, 50, 162–177. <https://doi.org/10.1016/j.advwatres.2012.06.005>
- Banta, R. M. (1995). Sea breezes shallow and deep on the California coast. *Monthly Weather Review*, 123(12), 3614–3622. [https://doi.org/10.1175/1520-0493\(1995\)123<3614:SBSADO>2.0.CO;2](https://doi.org/10.1175/1520-0493(1995)123<3614:SBSADO>2.0.CO;2)
- Beven, K. (2001). How far can we go in distributed hydrological modelling? *Hydrology and Earth System Sciences*, 5(1), 1–12. <https://doi.org/10.5194/hess-5-1-2001>
- Beven, K. (2006). A manifesto for the equifinality thesis. *Journal of Hydrology*, 320(1–2), 18–36. <https://doi.org/10.1016/j.jhydrol.2005.07.007>
- Biswas, A. (2014). Scaling analysis of soil water storage with missing measurements using the second-generation continuous wavelet transform. *European Journal of Soil Science*, 65(4), 594–604. <https://doi.org/10.1111/ejss.12145>
- Bolliger, J., Wagner, H. H., & Turner, M. G. (2007). Identifying and quantifying landscape patterns in space and time. *Landscape Series*, 177–194. https://doi.org/10.1007/978-1-4020-4436-6_12
- Boschetti, L., Roy, D. P., Giglio, L., Huang, H., Zubkova, M., & Humber, M. L. (2019). Global validation of the collection 6 MODIS burned area product. *Remote Sensing of Environment*, 235, 111490. <https://doi.org/10.1016/J.RSE.2019.111490>
- Chan, S. K., Bindlish, R., O'Neill, P., Jackson, T., Njoku, E., Dunbar, S., et al. (2018). Development and assessment of the SMAP enhanced passive soil moisture product. *Remote Sensing of Environment*, 204, 931–941. <https://doi.org/10.1016/J.RSE.2017.08.025>
- Chaney, N. W., Metcalfe, P., & Wood, E. F. (2016). HydroBlocks: A field-scale resolving land surface model for application over continental extents. *Hydrological Processes*, 30(20), 3543–3559. <https://doi.org/10.1002/hyp.10891>
- Chang, Y., Xiao, J., Li, X., Frolking, S., Zhou, D., Schneider, A., et al. (2021). Exploring diurnal cycles of surface urban heat island intensity in Boston with land surface temperature data derived from GOES-R geostationary satellites. *Science of the Total Environment*, 763, 144224. <https://doi.org/10.1016/j.scitotenv.2020.144224>
- Chen, F., & Avissar, R. (1994). The impact of land-surface wetness heterogeneity on mesoscale heat fluxes. *Journal of Applied Meteorology*, 33(11), 1323–1340. [https://doi.org/10.1175/1520-0450\(1994\)033<1323:tiolsw>2.0.co;2](https://doi.org/10.1175/1520-0450(1994)033<1323:tiolsw>2.0.co;2)
- Chen, W., Genton, M. G., & Sun, Y. (2021). Space-time covariance structures and models. *Annual Review of Statistics and Its Application*, 8(1), 191–215. <https://doi.org/10.1146/annurev-statistics-042720-115603>
- Cheng, W. Y. Y., & Cotton, W. R. (2004). Sensitivity of a cloud-resolving simulation of the genesis of a mesoscale convective system to horizontal heterogeneities in soil moisture initialization. *Journal of Hydrometeorology*, 5(5), 934–958. [https://doi.org/10.1175/1525-7541\(2004\)005<0934:SOACSO>2.0.CO;2](https://doi.org/10.1175/1525-7541(2004)005<0934:SOACSO>2.0.CO;2)
- Courault, D., Drobinski, P., Brunet, Y., Lacarrere, P., & Talbot, C. (2007). Impact of surface heterogeneity on a buoyancy-driven convective boundary layer in light winds. *Boundary-Layer Meteorology*, 124(3), 383–403. <https://doi.org/10.1007/s10546-007-9172-y>
- Cressie, N., & Huang, H. C. (1999). Classes of nonseparable, spatio-temporal stationary covariance functions. *Journal of the American Statistical Association*, 94(448), 1330–1339. <https://doi.org/10.1080/01621459.1999.10473885>
- Cressie, N., & Wikle, C. (2015). *Statistics for spatio-temporal data*. John Wiley & Sons, Ltd.
- Crosman, E. T., & Horel, J. D. (2010). Sea and lake breezes: A review of numerical studies. *Boundary-Layer Meteorology*, 137(1), 1–29. <https://doi.org/10.1007/s10546-010-9517-9>
- Crow, W. T., Huffman, G. J., Bindlish, R., & Jackson, T. J. (2009). Improving satellite-based rainfall accumulation estimates using spaceborne surface soil moisture retrievals. *Journal of Hydrometeorology*, 10(1), 199–212. <https://doi.org/10.1175/2008JHM986.1>
- Daly, C., Taylor, G., & Gibson, W. (1997). The Prism approach to mapping precipitation and emperature. In *10th AMS Conference on Applied Climatology* (Vol. 1, pp. 1–4). Retrieved from <http://citeserx.ist.psu.edu/viewdoc/download?doi=10.1.1.730.5725&rep=rep1&type=pdf>
- de Iaco, S. (2010). Space-time correlation analysis: A comparative study. *Journal of Applied Statistics*, 37(6), 1027–1041. <https://doi.org/10.1080/02664760903019422>
- Demel, S. S., & Du, J. (2015). Spatio-temporal models for some data sets in continuous space and discrete time. *Statistica Sinica*, 25(1), 81–98. <https://doi.org/10.5705/ss.2013.223w>
- Desai, A. R., Khan, A. M., Zheng, T., Paleri, S., Butterworth, B., Lee, T. R., et al. (2021). Multi-sensor approach for high space and time resolution land surface temperature. *Earth and Space Science*, 8(10), 1–18. <https://doi.org/10.1029/2021EA001842>
- Devadoss, J., Falco, N., Dafflon, B., Wu, Y., Franklin, M., Hermes, A., et al. (2020). Remote sensing-informed zonation for understanding snow, plant and soil moisture dynamics within a mountain ecosystem. *Remote Sensing*, 12(17), 2733. <https://doi.org/10.3390/RS12172733>
- Dickinson, R. E. (1995). Land-atmosphere interaction. *Reviews of Geophysics*, 33(2 S), 917–922. <https://doi.org/10.1029/95RG00284>
- Dommegent, D., & Latif, M. (2002). A cautionary note on the interpretation of EOFs. *Journal of Climate*, 15(2), 216–225. [https://doi.org/10.1175/1520-0442\(2002\)015<0216:ACNOTI>2.0.CO;2](https://doi.org/10.1175/1520-0442(2002)015<0216:ACNOTI>2.0.CO;2)
- Douglas, M. W. (1995). The summertime low-level jet over the Gulf of California. *Monthly Weather Review*, 123(8), 2334–2347. [https://doi.org/10.1175/1520-0493\(1995\)123<2334:TSLLJO>2.0.CO;2](https://doi.org/10.1175/1520-0493(1995)123<2334:TSLLJO>2.0.CO;2)
- Duffy, K., Vandal, T. J., & Nemani, R. R. (2022). Multisensor machine learning to retrieve high spatiotemporal resolution land surface temperature. *IEEE Access*, 10, 89221–89231. <https://doi.org/10.1109/ACCESS.2022.3198673>
- Entekhabi, D. (1995). Recent advances in land-atmosphere interaction research. *Reviews of Geophysics*, 33(2 S), 995–1003. <https://doi.org/10.1029/95RG01163>
- Entekhabi, D., Njoku, E. G., O'Neill, P. E., Kellogg, K. H., Crow, W. T., Edelstein, W. N., et al. (2010). The soil moisture active passive (SMAP) mission. *Proceedings of the IEEE*, 98(5), 704–716. <https://doi.org/10.1109/JPROC.2010.2043918>

- Faghmous, J. H., & Kumar, V. (2014). Spatio-temporal data mining for climate data: Advances, challenges, and opportunities. *Studies in Big Data*, 83–116. https://doi.org/10.1007/978-3-642-40837-3_3
- Fang, L., Yu, Y., Xu, H., & Sun, D. (2014). New retrieval algorithm for deriving land surface temperature from geostationary orbiting satellite observations. *IEEE Transactions on Geoscience and Remote Sensing*, 52(2), 819–828. <https://doi.org/10.1109/TGRS.2013.2244213>
- Fang, Z., Bogena, H., Kollet, S., Koch, J., & Vereecken, H. (2015). Spatio-temporal validation of long-term 3D hydrological simulations of a forested catchment using empirical orthogonal functions and wavelet coherence analysis. *Journal of Hydrology*, 529, 1754–1767. <https://doi.org/10.1016/J.JHYDROL.2015.08.011>
- Fisher, J. B., Lee, B., Purdy, A. J., Halverson, G. H., Dohlen, M. B., Cawse-Nicholson, K., et al. (2020). ECOSTRESS: NASA's next generation mission to measure evapotranspiration from the International Space Station. *Water Resources Research*, 56(4), e2019WR026058. <https://doi.org/10.1029/2019WR026058>
- Freitas, S. C., Trigo, I. F., Macedo, J., Barroso, C., Silva, R., & Perdigão, R. (2013). Land surface temperature from multiple geostationary satellites. *International Journal of Remote Sensing*, 34(9–10), 3051–3068. <https://doi.org/10.1080/01431161.2012.716925>
- Gentine, P., Massmann, A., Lintner, B. R., Hamed Aleomohammadi, S., Fu, R., Green, J. K., et al. (2019). Land-atmosphere interactions in the tropics - A review. *Hydrology and Earth System Sciences*, 23(10), 4171–4197. <https://doi.org/10.5194/hess-23-4171-2019>
- Gesch, D., Evans, G., Mauck, J., Hutchinson, J., & Carswell, W. J., Jr. (2010). *The National Map-Elevation National Elevation Dataset: U.S. Geological Survey fact sheet, Technical Report 2009–3053*. U.S. Geological Survey. Retrieved from http://www.usgs.gov/ngpo/ngp_liaisons.html
- Gneiting, T. (2002). Nonseparable, stationary covariance functions for space-time data. *Journal of the American Statistical Association*, 97(458), 590–600. <https://doi.org/10.1198/016214502760047113>
- Graf, A., Herbst, M., Weihermüller, L., Huisman, J. A., Prolingheuer, N., Bornemann, L., & Vereecken, H. (2012). Analyzing spatiotemporal variability of heterotrophic soil respiration at the field scale using orthogonal functions. *Geoderma*, 181–182, 91–101. <https://doi.org/10.1016/j.geoderma.2012.02.016>
- Guttorp, P., & Sampson, P. D. (1994). 20 Methods for estimating heterogeneous spatial covariance functions with environmental applications. *Handbook of Statistics*, 12, 661–689. [https://doi.org/10.1016/S0169-7161\(05\)80022-7](https://doi.org/10.1016/S0169-7161(05)80022-7)
- Haas, T. C. (1990a). Kriging and automated variogram modeling within a moving window. *Atmospheric Environment Part A, General Topics*, 24(7), 1759–1769. [https://doi.org/10.1016/0960-1686\(90\)90508-K](https://doi.org/10.1016/0960-1686(90)90508-K)
- Haas, T. C. (1990b). Lognormal and moving window methods of estimating acid deposition. *Journal of the American Statistical Association*, 85(412), 950–963. <https://doi.org/10.1080/01621459.1990.10474966>
- Hannachi, A., Jolliffe, I. T., & Stephenson, D. B. (2007). Empirical orthogonal functions and related techniques in atmospheric science: A review. *International Journal of Climatology*, 27(9), 1119–1152. <https://doi.org/10.1002/joc.1499>
- Hashimoto, H., Wang, W., Dungan, J. L., Li, S., Michaelis, A. R., Takenaka, H., et al. (2021). New generation geostationary satellite observations support seasonality in greenness of the Amazon evergreen forests. *Nature Communications*, 12(1), 684. <https://doi.org/10.1038/s41467-021-20994-y>
- Holzman, M. E., Rivas, R., & Bayala, M. (2014). Subsurface soil moisture estimation by VI-LST method. *IEEE Geoscience and Remote Sensing Letters*, 11(11), 1951–1955. <https://doi.org/10.1109/LGRS.2014.2314617>
- Homer, C., Dewitz, J., Yang, L., Jin, S., Danielson, P., Xian, G., et al. (2015). Completion of the 2011 national land cover database for the conterminous United States – Representing a decade of land cover change information. *Photogrammetric Engineering and Remote Sensing*, 81(5), 345–354.
- Hook, S., & Hulley, G. (2019). ECOSTRESS Land Surface Temperature and Emissivity Daily L2 Global 70 m V001. <https://doi.org/10.5067/ECOSTRESS/ECO2LSTE.001>
- Ignatov, A., Pennybacker, M., Gladkova, I., Petrenko, B., Jonasson, O., & Kihai, Y. (2019). GHRSST NOAA/STAR GOES-16 ABI L2P America Region SST v2.70 dataset (GDS version 2). <https://doi.org/10.25921/ayf6-c438>
- Katul, G., Lai, C. T., Schäfer, K., Vidakovic, B., Albertson, J., Ellsworth, D., & Oren, R. (2001). Multiscale analysis of vegetation surface fluxes: From seconds to years. *Advances in Water Resources*, 24(9–10), 1119–1132. [https://doi.org/10.1016/S0309-1708\(01\)00029-X](https://doi.org/10.1016/S0309-1708(01)00029-X)
- Katul, G., & Parlange, M. B. (1995). Analysis of land surface heat fluxes using the orthonormal wavelet approach. *Water Resources Research*, 31(11), 2743–2749. <https://doi.org/10.1029/95WR00003>
- Keen, C. S., & Lyons, W. A. (1978). Lake/land breeze circulations on the western shore of Lake Michigan. *Journal of Applied Meteorology*, 17(12), 1843–1855. [https://doi.org/10.1175/1520-0450\(1978\)017<1843:LBCTW>2.0.CO;2](https://doi.org/10.1175/1520-0450(1978)017<1843:LBCTW>2.0.CO;2)
- Kerr, Y., Waldteufel, P., Richaume, P., Wigneron, J. P., Ferrazzoli, P., Mahmoodi, A., et al. (2012). The SMOS soil moisture retrieval algorithm. *IEEE Transactions on Geoscience and Remote Sensing*, 50(5 PART 1), 1384–1403. <https://doi.org/10.1109/TGRS.2012.2184548>
- Kim, G., & Barros, A. P. (2002). Space-time characterization of soil moisture from passive microwave remotely sensed imagery and ancillary data. *Remote Sensing of Environment*, 81(2–3), 393–403. [https://doi.org/10.1016/S0034-4257\(02\)00014-7](https://doi.org/10.1016/S0034-4257(02)00014-7)
- Kindle, J. C., Hodur, R. M., Derada, S., Paduan, J. D., Rosenfeld, L. K., & Chavez, F. Q. (2002). A COAMPS™ reanalysis for the Eastern Pacific: Properties of the diurnal sea breeze along the central California coast. *Geophysical Research Letters*, 29(24), 1998–2001. <https://doi.org/10.1029/2002GL015566>
- Knist, S., Goergen, K., & Simmer, C. (2020). Effects of land surface inhomogeneity on convection-permitting WRF simulations over central Europe. *Meteorology and Atmospheric Physics*, 132(1), 53–69. <https://doi.org/10.1007/s00703-019-00671-y>
- Ko, A., Mascaro, G., & Vivoni, E. R. (2019). Strategies to improve and evaluate physics-based hyperresolution hydrologic simulations at regional basin scales. *Water Resources Research*, 55(2), 1129–1152. <https://doi.org/10.1029/2018WR023521>
- Koch, J., Jensen, K. H., & Stisen, S. (2015). Toward a true spatial model evaluation in distributed hydrological modeling: Kappa statistics, Fuzzy theory, and EOF-analysis benchmarked by the human perception and evaluated against a modeling case study. *Water Resources Research*, 51(2), 1225–1246. <https://doi.org/10.1002/2014WR016607>
- Koch, J., Mendiguren, G., Mariethoz, G., & Stisen, S. (2017). Spatial sensitivity analysis of simulated land surface patterns in a catchment model using a set of innovative spatial performance metrics. *Journal of Hydrometeorology*, 18(4), 1121–1142. <https://doi.org/10.1175/JHM-D-16-0148.1>
- Koch, J., Siemann, A., Stisen, S., & Sheffield, J. (2016). Spatial validation of large-scale land surface models against monthly land surface temperature patterns using innovative performance metrics. *Journal of Geophysical Research: Atmospheres*, 121(10), 5430–5452. <https://doi.org/10.1002/2015JD024482>
- Korres, W., Koyama, C. N., Fiener, P., & Schneider, K. (2010). Analysis of surface soil moisture patterns in agricultural landscapes using Empirical Orthogonal Functions. *Hydrology and Earth System Sciences*, 14(5), 751–764. <https://doi.org/10.5194/hess-14-751-2010>
- Kuusela, M., & Stein, M. L. (2018). Locally stationary spatio-temporal interpolation of Argo profiling float data. *Proceedings of the Royal Society A: Mathematical, Physical and Engineering Sciences*, 474(2220), 20180400. <https://doi.org/10.1098/rspa.2018.0400>

- Laherrère, J., & Sornette, D. (1998). Stretched exponential distributions in nature and economy: "Fat tails" with characteristic scales. *European Physical Journal B: Condensed Matter and Complex Systems*, 2(4), 525–539. <https://doi.org/10.1007/s100510050276>
- Levine, P. A., Randerson, J. T., Swenson, S. C., & Lawrence, D. M. (2016). Evaluating the strength of the land-atmosphere moisture feedback in Earth system models using satellite observations. *Hydrology and Earth System Sciences*, 20(12), 4837–4856. <https://doi.org/10.5194/hess-20-4837-2016>
- Li, H. T., Brunner, P., Kinzelbach, W., Li, W. P., & Dong, X. G. (2009). Calibration of a groundwater model using pattern information from remote sensing data. *Journal of Hydrology*, 377(1–2), 120–130. <https://doi.org/10.1016/j.jhydrol.2009.08.012>
- Li, K., Guan, K., Jiang, C., Wang, S., Peng, B., & Cai, Y. (2021). Evaluation of four new land surface temperature (LST) products in the U.S. corn belt: ECOSTRESS, GOES-R, Landsat, and Sentinel-3. *IEEE Journal of Selected Topics in Applied Earth Observations and Remote Sensing*, 14, 9931–9945. <https://doi.org/10.1109/JSTARS.2021.3114613>
- Li, Q., Yang, J., & Yang, L. (2021). Impact of urban roughness representation on regional hydrometeorology: An idealized study. *Journal of Geophysical Research: Atmospheres*, 126(4), e2020JD033812. <https://doi.org/10.1029/2020JD033812>
- Lyons, W. A. (1972). The climatology and prediction of the Chicago lake breeze. *Journal of Applied Meteorology*, 11(8), 1259–1270. [https://doi.org/10.1175/1520-0450\(1972\)011<1259:TCAPOT>2.0.CO;2](https://doi.org/10.1175/1520-0450(1972)011<1259:TCAPOT>2.0.CO;2)
- Ma, C. (2003). Spatio-temporal stationary covariance models. *Journal of Multivariate Analysis*, 86(1), 97–107. [https://doi.org/10.1016/S0047-259X\(02\)00014-3](https://doi.org/10.1016/S0047-259X(02)00014-3)
- Ma, C. (2005). Spatio-temporal variograms and covariance models. *Advances in Applied Probability*, 37(3), 706–725. <https://doi.org/10.1239/aap/1127483743>
- Mälicke, M., Hassler, S. K., Blume, T., Weiler, M., & Zehe, E. (2020). Soil moisture: Variable in space but redundant in time. *Hydrology and Earth System Sciences*, 24(5), 2633–2653. <https://doi.org/10.5194/hess-24-2633-2020>
- Martens, B., Miralles, D. G., Lievens, H., Van Der Schalie, R., De Jeu, R. A. M., Fernández-Prieto, D., et al. (2017). GLEAM v3: Satellite-based land evaporation and root-zone soil moisture. *Geoscientific Model Development*, 10(5), 1903–1925. <https://doi.org/10.5194/gmd-10-1903-2017>
- Matheron, G. (1989). *Estimating and choosing*. Springer-Verlag. <https://doi.org/10.1007/978-3-642-48817-7>
- Monahan, A. H., Fyfe, J. C., Ambaum, M. H. P., Stephenson, D. B., & North, G. R. (2009). Empirical orthogonal functions: The medium is the message. *Journal of Climate*, 22(24), 6501–6514. <https://doi.org/10.1175/2009JCLI3062.1>
- Montero, J.-M., Fernández-Avilés, G., & Mateu, J. (2015). *Spatial and spatio-temporal geostatistical modeling and kriging* (1st ed.). Wiley.
- Nicholson, S. E. (1988). Land surface atmosphere interaction: Physical processes and surface changes and their impact. *Progress in Physical Geography*, 12(1), 36–65. <https://doi.org/10.1177/03091333801200102>
- Ohashi, Y., & Kida, H. (2002). Effects of mountains and urban areas on daytime local-circulations in the Osaka and Kyoto regions. *Journal of the Meteorological Society of Japan*, 80(4), 539–560. <https://doi.org/10.2151/jmsj.80.539>
- Painter, T. H., Rittger, K., McKenzie, C., Slaughter, P., Davis, R. E., & Dozier, J. (2009). Retrieval of subpixel snow covered area, grain size, and albedo from MODIS. *Remote Sensing of Environment*, 113(4), 868–879. <https://doi.org/10.1016/j.rse.2009.01.001>
- Parinussa, R. M., Holmes, T. R. H., Wanders, N., Dorigo, W. A., & De Jeu, R. A. M. (2015). A preliminary study toward consistent soil moisture from AMSR2. *Journal of Hydrometeorology*, 16(2), 932–947. <https://doi.org/10.1175/JHM-D-13-0200.1>
- Petrenko, B., Ignatov, A., Kihai, Y., & Heidinger, A. (2010). Clear-sky mask for the advanced clear-sky processor for oceans. *Journal of Atmospheric and Oceanic Technology*, 27(10), 1609–1623. <https://doi.org/10.1175/2010JTECHA1413.1>
- Petrenko, B., Ignatov, A., Kihai, Y., Stroup, J., & Dash, P. (2014). Evaluation and selection of SST regression algorithms for JPSS VIIRS. *Journal of Geophysical Research: Atmospheres*, 119(8), 4580–4599. <https://doi.org/10.1002/2013JD020637>
- Pielke, R. A. (2001). Influence of the spatial distribution of vegetation and soils on the prediction of cumulus convective rainfall. *Reviews of Geophysics*, 39(2), 151–177. <https://doi.org/10.1029/1999RG000072>
- Polehampton, E., Cox, C., Smith, D., Ghent, D., Wooster, M., Xu, W., et al. (2022). Copernicus Sentinel-3 SLSTR Land User Handbook. Retrieved from <https://sentinel.esa.int/documents/247904/4598082/Sentinel-3-SLSTR-Land-Handbook.pdf>
- Risser, M. D., & Turek, D. (2020). Bayesian inference for high-dimensional nonstationary Gaussian processes. *Journal of Statistical Computation and Simulation*, 90(16), 2902–2928. <https://doi.org/10.1080/00949655.2020.1792472>
- Rudi, J., Pabel, R., Jager, G., Koch, R., Kunoth, A., & Bogena, H. (2010). Multiscale analysis of hydrologic time series data using the Hilbert-Huang transform. *Vadose Zone Journal*, 9(4), 925–942. <https://doi.org/10.2136/vzj2009.0163>
- Running, S., Mu, Q., Zhao, M., & Moreno, A. (2019). MOD16A2GF MODIS/Terra Net Evapotranspiration Gap-Filled 8-Day L4 Global 500 m SIN Grid V006 [Dataset]. NASA. <https://doi.org/10.5067/MODIS/MOD16A2GF.006>
- Rupp, D. E., Daly, C., Doggett, M. K., Smith, J. I., & Steinberg, B. (2022). Mapping an observation-based global solar irradiance climatology across the conterminous United States. *Journal of Applied Meteorology and Climatology*, 61(7), 857–876. <https://doi.org/10.1175/JAMC-D-21-0236.1>
- Santanello, J. A., Dirmeyer, P. A., Ferguson, C. R., Findell, K. L., Tawfik, A. B., Berg, A., et al. (2018). Land-atmosphere interactions the LoCo perspective. *Bulletin of the American Meteorological Society*, 99(6), 1253–1272. <https://doi.org/10.1175/BAMS-D-17-0001.1>
- Schepanski, K., Klüser, L., Heinold, B., & Tegen, I. (2015). Spatial and temporal correlation length as a measure for the stationarity of atmospheric dust aerosol distribution. *Atmospheric Environment*, 122, 10–21. <https://doi.org/10.1016/j.atmosenv.2015.09.034>
- Shi, L., & Bates, J. J. (2011). Three decades of intersatellite-calibrated High-Resolution Infrared Radiation Sounder upper tropospheric water vapor. *Journal of Geophysical Research*, 116(D4), 4108. <https://doi.org/10.1029/2010JD014847>
- Sills, D. M. L., Brook, J. R., Levy, I., Makar, P. A., Zhang, J., & Taylor, P. A. (2011). Lake breezes in the southern Great Lakes region and their influence during BAQS-Met 2007. *Atmospheric Chemistry and Physics*, 11(15), 7955–7973. <https://doi.org/10.5194/acp-11-7955-2011>
- Simon, J. S., Bragg, A. D., Dirmeyer, P. A., & Chaney, N. W. (2021). Semi-coupling of a field-scale resolving land-surface model and WRF-LES to investigate the influence of land-surface heterogeneity on cloud development. *Journal of Advances in Modeling Earth Systems*, 13(10), e2021MS002602. <https://doi.org/10.1029/2021MS002602>
- Sims, D. A., Rahman, A. F., Cordova, V. D., El-Masri, B. Z., Baldocchi, D. D., Bolstad, P. V., et al. (2008). A new model of gross primary productivity for North American ecosystems based solely on the enhanced vegetation index and land surface temperature from MODIS. *Remote Sensing of Environment*, 112(4), 1633–1646. <https://doi.org/10.1016/j.rse.2007.08.004>
- Sobrino, J. A., Li, Z. L., & Stoll, M. P. (1993). Impact of the atmospheric transmittance and total water vapor content in the algorithms for estimating satellite sea surface temperatures. *IEEE Transactions on Geoscience and Remote Sensing*, 31(5), 946–952. <https://doi.org/10.1109/36.263765>
- Stein, M. L. (1999). *Interpolation of spatial data: Some theory for kriging*. Springer.
- Stein, M. L. (2005). Space-time covariance functions. *Journal of the American Statistical Association*, 100(469), 310–321. <https://doi.org/10.1198/016214504000000854>

- Stein, M. L. (2020). Some statistical issues in climate science. *Statistical Science*, 35(1), 31–41. <https://doi.org/10.1214/19-STS730>
- Stisen, S., McCabe, M. F., Refsgaard, J. C., Lerer, S., & Butts, M. B. (2011). Model parameter analysis using remotely sensed pattern information in a multi-constraint framework. *Journal of Hydrology*, 409(1–2), 337–349. <https://doi.org/10.1016/j.jhydrol.2011.08.030>
- Stisen, S., Soltani, M., Mendiguren, G., Langkilde, H., Garcia, M., & Koch, J. (2021). Spatial patterns in actual evapotranspiration climatologies for Europe. *Remote Sensing*, 13(12), 2410. <https://doi.org/10.3390/rs13122410>
- Stoy, P. C., Katul, G., Siqueira, M. B. S., Juang, J. Y., McCarthy, H. R., Kim, H. S., et al. (2005). Variability in net ecosystem exchange from hourly to inter-annual time scales at adjacent pine and hardwood forests: A wavelet analysis. *Tree Physiology*, 25(7), 887–902. <https://doi.org/10.1093/treephys/25.7.887>
- Su, Z. (2002). The Surface Energy Balance System (SEBS) for estimation of turbulent heat fluxes. *Hydrology and Earth System Sciences*, 6(1), 85–99. <https://doi.org/10.5194/hess-6-85-2002>
- Tapley, B. D., Bettadpur, S., Ries, J. C., Thompson, P. F., & Watkins, M. M. (2004). GRACE measurements of mass variability in the Earth system. *Science*, 305(5683), 503–505. https://doi.org/10.1126/SCIENCE.1099192/SUPPL_FILE/TAPLEY_SOM.PDF
- Taylor, C. M., Parker, D. J., & Harris, P. P. (2007). An observational case study of mesoscale atmospheric circulations induced by soil moisture. *Geophysical Research Letters*, 34(15), L15801. <https://doi.org/10.1029/2007GL030572>
- Tobler, W. R. (1970). A computer movie simulating urban growth in the Detroit region. *Economic Geography*, 46, 234. <https://doi.org/10.2307/143141>
- Torres-Rojas, L., & Chaney, N. W. (2023). Supporting Dataset: The observed spatio-temporal patterns of Land surface temperature over the Contiguous United States [Dataset]. *Zenodo*. <https://doi.org/10.5281/ZENODO.8428629>
- Townshend, J. (2016). Global Forest Cover Change (GFCC) Tree Cover Multi-Year Global 30 m V003 [Dataset]. NASA EOSDIS Land Processes Distributed Active Archive Center. <https://doi.org/10.5067/MEaSUREs/GFCC/GFCC30TC.003>
- Tsai, Y.-L. S., Dietz, A., Oppelt, N., & Kuenzer, C. (2019). Remote sensing of snow cover using spaceborne SAR: A review. *Remote Sensing*, 11(12), 1456. <https://doi.org/10.3390/RS11121456>
- Turnipseed, A. A., Anderson, D. E., Burns, S., Blanken, P. D., & Monson, R. K. (2004). Airflows and turbulent flux measurements in mountainous terrain: Part 2: Mesoscale effects. *Agricultural and Forest Meteorology*, 125(3–4), 187–205. <https://doi.org/10.1016/j.agrformet.2004.04.007>
- Tuttle, S., & Salvucci, G. (2016). Empirical evidence of contrasting soil moisture–precipitation feedbacks across the United States. *Science*, 352(6287), 825–828. <https://doi.org/10.1126/science.aaa7185>
- van der Meer, F. (2012). Remote-sensing image analysis and geostatistics. *International Journal of Remote Sensing*, 33(18), 5644–5676. <https://doi.org/10.1080/01431161.2012.666363>
- Vargas, R., Detto, M., Baldocchi, D. D., & Allen, M. F. (2010). Multiscale analysis of temporal variability of soil CO₂ production as influenced by weather and vegetation. *Global Change Biology*, 16(5), 1589–1605. <https://doi.org/10.1111/j.1365-2486.2009.02111.x>
- Vereecken, H., Huisman, J. A., Bogena, H., Vanderborght, J., Vrugt, J. A., & Hopmans, J. W. (2008). On the value of soil moisture measurements in vadose zone hydrology: A review. *Water Resources Research*, 46(4), W00D06. <https://doi.org/10.1029/2008WR006829>
- Vereecken, H., Pachepsky, Y., Simmer, C., Rihani, J., Kunoth, A., Korres, W., et al. (2016). On the role of patterns in understanding the functioning of soil-vegetation-atmosphere systems. *Journal of Hydrology*, 542, 63–86. <https://doi.org/10.1016/j.jhydrol.2016.08.053>
- Wagner, D., Ruprecht, E., & Simmer, C. (1990). A combination of microwave observations from satellites and an EOF analysis to retrieve vertical humidity profiles over the ocean. *Journal of Applied Meteorology*, 29(11), 1142–1157. [https://doi.org/10.1175/1520-0450\(1990\)029<1142:ACOMOF>2.0.CO;2](https://doi.org/10.1175/1520-0450(1990)029<1142:ACOMOF>2.0.CO;2)
- Wagner, J. S., Gohm, A., & Rotach, M. W. (2015). The impact of valley geometry on daytime thermally driven flows and vertical transport processes. *Quarterly Journal of the Royal Meteorological Society*, 141(690), 1780–1794. <https://doi.org/10.1002/qj.2481>
- Wagner, W., Hahn, S., Kidd, R., Melzer, T., Bartalis, Z., Hasenauer, S., et al. (2013). The ASCAT soil moisture product: A review of its specifications, validation results, and emerging applications. *Meteorologische Zeitschrift*, 22(1), 5–33. <https://doi.org/10.1127/0941-2948/2013/0399>
- Wainwright, H. M., Uhlemann, S., Franklin, M., Falco, N., Bouskill, N. J., Newcomer, M. E., et al. (2022). Watershed zonation through hillslope clustering for tractably quantifying above-and below-ground watershed heterogeneity and functions. *Hydrology and Earth System Sciences*, 26(2), 429–444. <https://doi.org/10.5194/hess-26-429-2022>
- Wan, Z. (2014). New refinements and validation of the collection-6 MODIS land-surface temperature/emissivity product. *Remote Sensing of Environment*, 140, 36–45. <https://doi.org/10.1016/J.RSE.2013.08.027>
- Wan, Z., & Dozier, J. (1996). A generalized split-window algorithm for retrieving land-surface temperature from space. *IEEE Transactions on Geoscience and Remote Sensing*, 34(4), 892–905. <https://doi.org/10.1109/36.508406>
- Wang, K., & Dickinson, R. E. (2012). A review of global terrestrial evapotranspiration: Observation, modeling, climatology, and climatic variability. *Reviews of Geophysics*, 50(2), 2005. <https://doi.org/10.1029/2011RG000373>
- Wang, Y., Di Sabatino, S., Martilli, A., Li, Y., Wong, M. S., Gutiérrez, E., & Chan, P. W. (2017). Impact of land surface heterogeneity on urban heat island circulation and sea-land breeze circulation in Hong Kong. *Journal of Geophysical Research: Atmospheres*, 122(8), 4332–4352. <https://doi.org/10.1002/2017JD026702>
- Wealands, S. R., Grayson, R. B., & Walker, J. P. (2005). Quantitative comparison of spatial fields for hydrological model assessment - Some promising approaches. *Advances in Water Resources*, 28(1), 15–32. <https://doi.org/10.1016/j.advwatres.2004.10.001>
- Weaver, C. P. (2004). Coupling between large-scale atmospheric processes and mesoscale land-atmosphere interactions in the U.S. Southern Great Plains during summer. Part I: Case studies. *Journal of Hydrometeorology*, 5(6), 1223–1246. <https://doi.org/10.1175/JHM-396.1>
- Whiteman, C. D., Hoch, S. W., & Poulos, G. S. (2009). Evening temperature rises on valley floors and slopes: Their causes and their relationship to the thermally driven wind system. *Journal of Applied Meteorology and Climatology*, 48(4), 776–788. <https://doi.org/10.1175/2008JAMC2028.1>
- Wikle, C. K. (2015). Modern perspectives on statistics for spatio-temporal data. *Wiley Interdisciplinary Reviews: Computational Statistics*, 7(1), 86–98. <https://doi.org/10.1002/wics.1341>
- Wilson, A. M., & Barros, A. P. (2015). Landform controls on low level moisture convergence and the diurnal cycle of warm season orographic rainfall in the Southern Appalachians. *Journal of Hydrology*, 531, 475–493. <https://doi.org/10.1016/j.jhydrol.2015.10.068>
- Wu, C., Lo, M., Chen, W., & Lu, C. (2015). The impacts of heterogeneous land surface fluxes on the diurnal cycle precipitation: A framework for improving the GCM representation of land-atmosphere interactions. *Journal of Geophysical Research: Atmospheres*, 120(9), 3714–3727. <https://doi.org/10.1002/2014JD023030>
- Wu, Z., Feng, J., Qiao, F., & Tan, Z. M. (2016). Fast multidimensional ensemble empirical mode decomposition for the analysis of big spatio-temporal datasets. *Philosophical Transactions of the Royal Society A: Mathematical, Physical and Engineering Sciences*, 374(2065), 20150197. <https://doi.org/10.1098/rsta.2015.0197>

- Xiao, M., Mascaro, G., Wang, Z., Whitney, K. M., & Vivoni, E. R. (2022). On the value of satellite remote sensing to reduce uncertainties of regional simulations of the Colorado River. *Hydrology and Earth System Sciences*, 26(21), 5627–5646. <https://doi.org/10.5194/hess-26-5627-2022>
- Xu, F., & Ignatov, A. (2014). In situ SST quality monitor (iQuam). *Journal of Atmospheric and Oceanic Technology*, 31(1), 164–180. <https://doi.org/10.1175/JTECH-D-13-00121.1>
- Yu, Y., Tarpley, D., Hui, X., & Chen, M. (2012). *GOES-R Advanced Baseline Imager (ABI) Algorithm Theoretical Basis Document for Land Surface Temperature (Version 2)*. NOAA NESDIS, Center for Satellite Applications and Research.
- Yu, Y., & Yu, P. (2020). Land Surface Temperature Product from the GOES-R Series. In *The GOES-R Series* (pp. 133–144). Elsevier. <https://doi.org/10.1016/B978-0-12-814327-8.00012-3>
- Zakeri, F., & Mariethoz, G. (2021). A review of geostatistical simulation models applied to satellite remote sensing: Methods and applications. *Remote Sensing of Environment*, 259, 112381. <https://doi.org/10.1016/j.rse.2021.112381>
- Zardi, D., & Whiteman, C. D. (2013). Diurnal Mountain Wind Systems. In F. Chow, S. De Wekker, & B. Snyder (Eds.), *Mountain Weather Research and Forecasting* (pp. 35–119). Springer Atmospheric Sciences. https://doi.org/10.1007/978-94-007-4098-3_2
- Zheng, Y., Brunsell, N. A., Alfieri, J. G., & Niyogi, D. (2021). Impacts of land cover heterogeneity and land surface parameterizations on turbulent characteristics and mesoscale simulations. *Meteorology and Atmospheric Physics*, 133(3), 589–610. <https://doi.org/10.1007/s00703-020-00768-9>
- Zink, M., Mai, J., Cuntz, M., & Samaniego, L. (2018). Conditioning a hydrologic model using patterns of remotely sensed land surface temperature. *Water Resources Research*, 54(4), 2976–2998. <https://doi.org/10.1002/2017WR021346>
- Zuidema, P., Fairall, C., Hartten, L. M., Hare, J. E., & Wolfe, D. (2007). On air-sea interaction at the mouth of the Gulf of California. *Journal of Climate*, 20(9), 1649–1661. <https://doi.org/10.1175/JCLI4089.1>